



UNIVERSIDAD DE CONCEPCIÓN
FACULTAD DE CIENCIAS FÍSICAS Y MATEMÁTICAS

A WISE VIEW OF GALAXIES
WITHIN PROTO-CLUSTER
CANDIDATES



Tesis presentada a la Facultad de Ciencias Físicas y Matemáticas de la
Universidad de Concepción para optar al grado académico de Magíster en
Astronomía

Por: Caleb Mauricio Gatica Ilufi

Profesor Guía: Ricardo Demarco

Octubre 2022
Concepción, Chile



© 2022, Caleb Mauricio Gatica Ilufi

Se autoriza la reproducción total o parcial, con fines académicos, por cualquier medio o procedimiento, incluyendo la cita bibliográfica del documento

AGRADECIMIENTOS

En este espacio, quiero agradecer primeramente a mis padres María Isabel Ilufi y Wenceslao Gatica Díaz (Q. E. P. D.) por brindarme su amor incondicional y la educación. A mis hermanos y hermana, por cada uno de sus consejos de vida. Quiero agradecer a mi pareja, por su amor y apoyo inamovibles. Agradezco también a mis amigos, compañeras y compañeros, con quienes he compartido grandes y bellos momentos, presencial y remotamente. A todas estas personas les agradezco, por que me han hecho la persona que soy hoy en día. Cada uno de ellos representa una parte del pilar que me sostiene.

Agradezco también a Ricardo, mi supervisor, por sus consejos y guía académica. También a los profesores del departamento de astronomía que con dedicación nos enseñan sus conocimientos.

Agradezco además, a mi colaboración: Hervé Dole, Mari Polletta, Brenda Frye, Clement Martinache y Alessandro Rettura. Por sus útiles comentarios y contribuciones que aportaron en mejorar la calidad de este trabajo.

Finalmente agradezco el apoyo financiero que me ha brindado la Universidad de Concepción a través de la beca de arancel.

Resumen

Una completa comprensión de la historia de la formación y ensamblaje de masa en las estructuras en el universo requiere de estudiar el crecimiento de las galaxias y sus agujeros negros supermasivos (SMBHs, por sus siglas en inglés) en función de su ambiente local a lo largo del tiempo cósmico. Bajo este contexto, un aspecto importante es cuantificar los efectos que causan las etapas tempranas del desarrollo de cúmulos de galaxias en el crecimiento de los SMBHs. Para esto, hemos estimado la fracción de galaxias de núcleo activo (AGN) de una, relativamente, gran muestra de galaxias pertenecientes a candidatos de protocúmulos (PCs). Éstos corresponden a una muestra de fuentes observada con el instrumento SPIRE del telescopio espacial Herschel, de aproximadamente 228 fuentes rojas y compactas, seleccionadas con el telescopio espacial Planck. Estimamos la fracción de AGN usando la fotometría de alta resolución en el infrarrojo medio (mid-IR) que nos proporcionan los datos de WISE/AllWISE de aproximadamente 650 fuentes homólogas, en el rango de redshifts fotométrico $1 \lesssim z \lesssim 3$. Creamos un clasificador basado en colores de las bandas de WISE en $3.4 \mu\text{m}$ (W1), $4.6 \mu\text{m}$ (W2) y $12 \mu\text{m}$ (W3). Para clasificar robustamente las fuentes AGN utilizamos un algoritmo de aprendizaje de máquina de *clustering* y un corte de color en $\text{W1} - \text{W2} > 0.721$ en la creación de nuestro clasificador. La incertidumbre de la fracción de AGN fue estimada bajo una aproximación de Monte Carlo. Para un mejor entendimiento de la influencia del ambiente en el desarrollo de las galaxias, comparamos la fracción de AGN en PCs con la fracción de AGN en el campo. Encontramos una fracción de AGN de $f_{\text{AGN}} = 0.167 \pm 0.03$ en los candidatos a PCs y una fracción de AGN de $f_{\text{AGN}} = 0.123 \pm 0.015$ en el campo. De nuestro catálogo, seleccionamos una sub-muestra mas roja (esto es, con razones de flujo $S_{350\mu\text{m}}/S_{250\mu\text{m}} > 0.7$ y $S_{500\mu\text{m}}/S_{350\mu\text{m}} > 0.6$) que presenta una sobredensidad de mayor significancia, la cual resulta con una fracción de AGN de $f_{\text{AGN}} = 0.283 \pm 0.049$, lo que es consistente con fracciones de AGN más altas para ambientes más densos. Concluimos que nuestros resultados apuntan a una alta fracción de AGN en ambientes de PCs, y son compatibles con otros estudios. Sin embargo, es difícil profundizar y obtener mayores conclusiones respecto de la actividad de AGNs a estos altos redshifts.

Keywords – galaxias: activa – galaxias: alto redshift – galaxias: cúmulos –

general: infrarrojo



Abstract

A complete understanding of the mass assembly history of structures in the universe requires the study of the growth of galaxies and their super-massive black holes (SMBHs) as a function of their local environment over cosmic time. In this context, an important aspect is to quantify the effects that the early stages of galaxy cluster development have on the growth of SMBHs. For this, we have used a sample of Herschel/SPIRE sources of ~ 228 red and compact Planck selected sources which are protocluster (PC) candidates to estimate the active galactic nuclei (AGN) fraction from a relatively large sample of galaxies within these candidates. We estimate the AGN fraction by using the high resolution mid-Infrared (mid-IR) photometry provided by the WISE/AllWISE data of ~ 650 counterparts within the $1 \lesssim z \lesssim 3$ (photometric) redshift range. We created an AllWISE mid-IR colour-colour selection using a clustering machine learning algorithm and a *WISE* colour cut using the $3.4 \mu m$ (W1) and $4.6 \mu m$ (W2) passbands, $W1 - W2 > 0.721$, to robustly classify sources as having AGN. We estimate the AGN fraction uncertainty by a Monte Carlo approach. We also compare the AGN fraction in PCs with that in the field to better understand the influence of the environment on galaxy development. We found an AGN fraction of $f_{AGN} = 0.167 \pm 0.03$ in PC candidates and an AGN fraction of $f_{AGN} = 0.123 \pm 0.015$ in the field. Out of our catalogue, we selected a “redder” ($S_{350\mu m}/S_{250\mu m} > 0.7$ and $S_{500\mu m}/S_{350\mu m} > 0.6$) SPIRE subsample with a higher overdensity significance, with a resulting AGN fraction of $f_{AGN} = 0.283 \pm 0.049$, consistent with higher AGN fractions for denser environments. We conclude that our results point towards a higher AGN fraction in PCs and are compatible with other studies. It is difficult to reach further conclusions regarding AGN activity at these high redshifts.

Keywords – galaxies: active – galaxies: high-redshift – galaxies: clusters – general: infrared

Contents

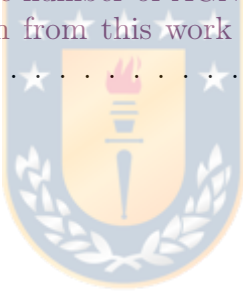
AGRADECIMIENTOS	i
Resumen	ii
Abstract	iv
1 Introduction	1
1.1 Protoclusters and galaxy evolution	1
1.2 Thesis objective	6
2 Data and Catalogs	7
2.1 Overview	7
2.2 Main sample	7
2.2.1 Planck XXVII	7
2.2.2 Planck XXVII WISE counterparts	10
2.3 Control Sample	14
2.3.1 AGN	14
2.3.2 SF/non-AGN galaxies	16
2.3.3 Balanced Control Sample	16
3 Methodology	18
3.1 AGN classification	18
3.1.1 Building the classifier	19
3.1.2 Testing	20
3.1.3 Monte Carlo simulation	20
4 Results	24
4.1 Classification of the SPIRE sources	24
4.2 AGN fractions	26
5 Discussion and Conclusions	30
5.1 Discussion	30
5.1.1 AGN selection	30
5.1.2 AGN fraction and their implications in protoclusters	32
5.2 Conclusions	33

Referencias	36
-------------	-----------



List of Tables

2.3.1 Summary of our final control sample. For each catalogue we show the type of galaxy selected, the number of sources and the corresponding reference.	16
4.1.1 Classification result of the SPIRE WISE counterparts.	24
5.1.1 Ratio of AGN classifications following this work and Assef et al. (2018) and the true number of AGN. General comparison between AGN classification from this work and classification from Assef et al. (2018).	32



List of Figures

1.1.1 NIR observations of UltraVISTA K_s band ($6' \times 6'$) for the protocluster PHz G237.01+42.50. The $4' \times 4'$ black square shows the region in which spectroscopic images will be taken with the LUCI spectrograph. The red rectangles ($1'' \times 8\text{--}10''$) show the slits for each target and yellow squares show alignment stars. The SPIRE positions are shown with the cyan circles of $11''$. Also, Planck red-excess contours are shown in purple, at the levels of 50, 62.5, 75 and 87.5% of the highest value. Figure taken from Polletta et al. (2021).	2
1.1.2 History of cosmic star formation, derived with FUV+IR rest-frame measurements, from Madau and Dickinson (2014). This figure clearly shows the peak around redshift $z \sim 2 - 3$. Different colors denote different observations, while the black line shows the best fit.	4
1.1.3 AGN fractions in protoclusters (filled symbols) and field galaxies (empty symbols), as a function of redshift. Here it is shown how the AGN fraction is lower in PCs for $z < 1$, comparable at $1 < z < 1.5$, and usually higher at $z < 2$, with Macuga et al. 2019 results (black symbols) as an exception. Red symbols are measurements using emission lines, green symbols denote measurements using broadband colors and purple and blue show averages for large samples of clusters.	5
2.2.1 A 20×16 arcmin 2 WISE observation at $4.6\mu m$ (W2 band) of one of our PC candidates, PLCK_HZ_G086.1plus61.6, shown as an example. The yellow contours show emission levels at 2σ and 3σ of the Herschel/SPIRE observation at $500\mu m$, for the same field. The red contour corresponds to the 50% of the peak flux of the respective Planck image at 545 GHz, that separates the “in” and “out” regions. WISE “in” and “out” sources are enclosed by magenta and cyan circles, respectively. The sources enclosed by a blue star were classified as AGN according to our method (see Section 3.1).	9
2.2.2 Flux densities of WISE sources at $SNR \geq 7$ in Planck fields of SPIRE sources. Blue, green, yellow and red colours correspond to W1, W2, W3 and W4 bands, respectively.	11

2.2.3 Completeness of AllWISE catalogue as a function flux density, for the bands W1, W2, W3 and W4.	13
2.2.4 W1-W2 vs. W2-W3 colour-colour diagram of the WISE counterparts for the SPIRE sources. Purple and cyan dots show the sources that are “in” and “out” of the Planck 50% intensity region, respectively. The “in” display the same spread in colours as the sources in the “out” region. The over plotted contours show color distribution for our control sample in the 1, 1.5 and 2σ levels. Blue contours show the distribution for AGN sources, while the red show the non-AGN sources. Our control sample is used to train and test our classifier (see Section 3.1) and includes 614 AGN from the Véron-Cetty and Véron (2010) and the Secrest et al. (2015) catalogues, and 636 SF/non-AGN from the Chang et al. (2015) and Kashino et al. (2019) catalogues (see Section 2.3). We see that most of the SPIRE sources have colours in the same range of the colours from the control sample. The AGN distribution tends to be redder in the W1-W2 colour and bluer in the W2-W3 colour when compared to SF/non-AGN galaxies.	15
3.1.1 Confusion matrices of our classification test with a 188 sources test sample. Each matrix shows the number of true positives (top left), false negatives (top right), false positives (bottom left) and true negatives (bottom right). <i>Left panel:</i> Confusion matrix for the classifier without adding the colour cut at $W1-W2 = 0.721$. The accuracy of the classification is of 82%, with 97% completeness and 77% reliability. <i>Right panel:</i> Confusion Matrix for the classifier, now adding the colour cut at $W1-W2 = 0.721$. The accuracy of the classification using the colour cut increases to an 88.8%, with 99% completeness and 83% reliability.	20
3.1.2 SPIRE WISE counterparts distributions for the W2-W3 (left panel) and W1-W2 (right panel) colours. Purple and cyan colours represent sources flagged as <i>in</i> and <i>out</i> , respectively. The green and blue dashed curves show the interpolation to the <i>in</i> and <i>out</i> distributions. We used these interpolations to generate the simulated data for the Monte Carlo simulation (used to estimate the uncertainty of the classifier).	21
3.1.3 Example of simulated data for one iteration of the Monte Carlo simulation. The figure shows the colour-colour diagram for W1-W2 as a function of W2-W3. Purple and cyan colours represent sources flagged as <i>in</i> and <i>out</i> , respectively. Here we show that the simulated data follow a similar colour-colour distribution than the SPIRE’s one, shown in Figures 2.2.4 and 3.1.2.	22

- 3.1.4 Resulting normal distributions (red) for the 10,000-step Monte Carlo simulation of the AGN fractions for sources inside (top left panel) and outside (top right panel) PCs. The normal distributions for the Monte Carlo simulations for out redder subsample (bottom left panel) and for the HerMES field sample (bottom right panel) are also shown. The solid black line shows a fitted gaussian model, with its corresponding mean (dashed black line) and standard deviation (shaded gray region). From these normal distribution, we use the $1-\sigma$ standard deviation as our AGN fractions uncertainties. This is, the AGN fraction for “in” sources has an error of 0.030, the AGN fraction for “out” sources has an error of 0.015, the AGN fraction of the redder sample has an error of 0.049 and the AGN fraction of the HerMES sample has en error of 0.007.

23

4.1.1 Classification result for the SPIRE sources (green) in the W1-W2 vs. W2-W3 colour-colour diagram. To consider a source as an AGN, two conditions must be met. The source must be located: (1) above the black horizontal line, which corresponds to a $3-\sigma$ level threshold for AGN in W1-W2 colour, and (2) over the red background area of the colour-colour diagram, which corresponds to the AGN classification given by the *k-means* separation. Filled (empty) stars represent the sources inside (outside) the PCs that were classified as AGN. Filled (empty) circles are the sources inside (outside) the PCs classified as non-AGN. The blue and red contours show the 1, 1.5 and $2-\sigma$ levels of the AGN and SF/non-AGN sources in the training data set of our control sample, respectively. This shows that both our main sample and control sample have a similar colour range covered. The upper panel shows the histogram distribution for the W2-W3 colour for the SPIRE sources (green), and for the AGN sources (blue) and the SF/non-AGN sources (red) of the control sample. Similarly, the right side panel shows the histogram of those distributions for the W1-W2 colour, including the $3-\sigma$ level threshold shown as the solid black line. The different coloured dashed lines show the fitted gaussian model for each distribution.

25

4.2.1 Figure taken from (Planck Collaboration et al., 2015). Left panel shows the cumulative overdensity for their Planck fields, using $350\mu\text{m}$ SPIRE sources. Right panel shows the normalized cumulative number of sources as a function of the statistical significance in σ from the density maps. This indicates how the red sources have a higher overdensity significance.

26

4.2.2 Figure taken from (Planck Collaboration et al., 2015). This figure shows the source density as a function of the colors S_{350}/S_{250} (left panel) and S_{500}/S_{350} (right panel), for different fields. It is shown how the subsample of "in" sources is higher than other fields.

27

4.2.3 AGN fractions, f_{AGN} , for the red SPIRE sources (cyan), SPIRE sources that are inside PC (blue), outside PC (red) and HerMES field (dark red) versus redshift. For easier visualization, we show the 1- σ significance of the AGN fractions as boxes in arbitrary redshift positions. Literature values from Polletta et al. (2021) (black star) and Macuga et al. (2019, and references therein; black circle, triangle, square and diamond) are added as reference for cluster/PC (filled black markers) and field (empty grey markers) galaxies. Here we show that the AGN fraction is, in general, greater in PCs than in the field. See also Figure 4.2.4.	28
4.2.4 AGN fractions, f_{AGN} (and 1- σ significance), for the red SPIRE sources (cyan), SPIRE sources that are inside PC (blue), outside PC (red) and HerMES field (dark red). Literature values from Polletta et al. (2021) and Macuga et al. (2019, and references therein) are added as reference for cluster/PC (filled stars) and field (empty stars) galaxies. The arbitrary y-axis was chosen to better distinguish the difference in the AGN fractions, taking into account their significance. See also Figure 4.2.3.	29
5.1.1 Comparison of AGN selection criteria between this work and Assef et al. (2018). In the left (right) panel we show the colour-colour distribution of our control (SPIRE) sample (grey dots). The dashed black line shows our AGN selection criterion, while up- and down-pointing triangles correspond to sources selected as AGN following Assef et al. (2018) for R90 and R75, respectively. The AGN selected sources are colour coded for W2 magnitude. The majority of our AGN selected data, 109% from the control sample, 84% from the all SPIRE sample, and 95% from the red SPIRE sources were also selected as AGN following Assef et al. (2018)'s criteria, principally for R90.	31

Chapter 1

Introduction

1.1 Protoclusters and galaxy evolution

When studying galaxies in the Universe we see that they are not randomly distributed in space. Instead, some of them are part of large gravitationally-bound structures, galaxy clusters (e.g. [Oort 1983](#); [Waldrop 1983](#)).

Observations show that cluster galaxies exhibit properties that are different from those of their counterparts in the field. Particularly, they usually have shorter star formation timescales (faster evolution) and lower star formation rates (SFRs) both of which depend on mass (e.g. [Poggianti et al. 1999](#); [Demarco et al. 2010](#); [Rettura et al. 2010](#)). This raises important questions on what are the differences between galaxies as a function of their environment and how their evolutionary paths vary over cosmic time from the first density fluctuations to local current structures. To answer these questions, it is necessary to study galaxies that belong to the progenitor structures of today's massive clusters called protoclusters (PCs).

For example, Figure 1.1.1 shows near-infrared (NIR) observations of the protocluster PHz G237.01+42.50, which is at redshift $z=2.16$.

These structures need to be studied during an epoch when these galaxies formed the bulk of their stars ([Muldrew et al., 2015](#); [Overzier, 2016](#)). This means that we need to identify and characterize PCs at high redshift at $z \sim 2 - 3$ ("cosmic noon"), which corresponds to the time in cosmic history when the peak of the Universe's SFR density occurs ([Madau and Dickinson, 2014](#), for a review).

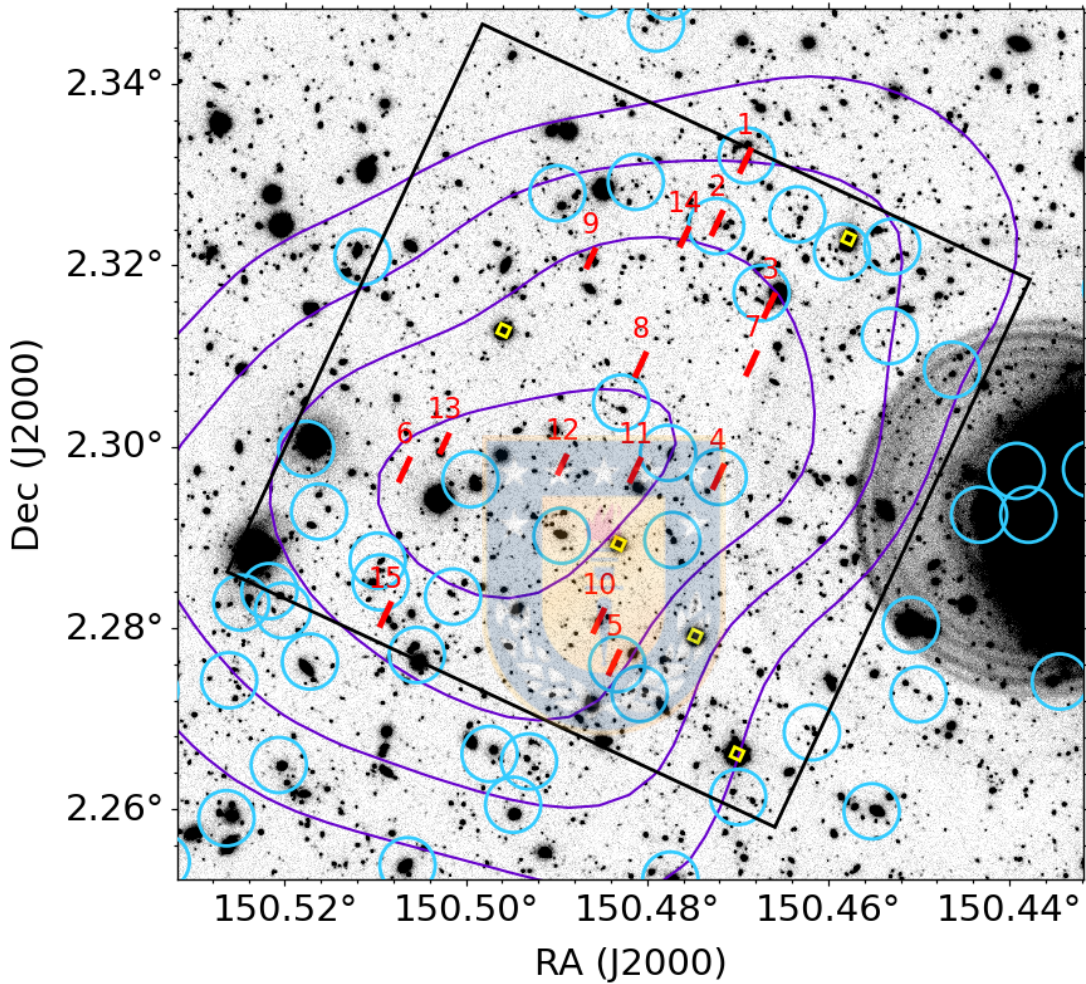


Figure 1.1.1: NIR observations of UltraVISTA K_s band ($6' \times 6'$) for the protocluster PHz G237.01+42.50. The $4' \times 4'$ black square shows the region in which spectroscopic images will be taken with the LUCI spectrograph. The red rectangles ($1'' \times 8-10''$) show the slits for each target and yellow squares show alignment stars. The SPIRE positions are shown with the cyan circles of $11''$. Also, Planck red-excess countours are shown in purple, at the levels of 50, 62.5, 75 and 87.5% of the highest value. Figure taken from Polletta et al. (2021).

Figure 1.1.2 shows the history of cosmic star formation from [Madau and Dickinson \(2014\)](#), and how it peaks around those redshifts.

In order to be able to provide a complete picture of galaxy evolution as large scale structures assemble and develop, we must understand the simultaneous growth of galaxies and their super-massive black holes (SMBHs). The active growth of a SMBH in a galaxy is typically signaled during its most vigorous phases of mass accretion (active galactic nucleus; AGN).

There is clear evidence that the occurrence of AGN in the Universe has a peak also at the above redshift interval of $z \sim 2 - 3$ (e.g. [Hasinger et al. 2005](#); [Bongiorno et al. 2007](#); [Fanidakis et al. 2012](#)), although this is the case of non-obscured AGN. The first stages of SMBH growth may well be occurring hidden from view at higher redshifts in dust-obscured galaxy mergers ([Piconcelli et al., 2015](#); [Wu et al., 2018](#); [Díaz-Santos et al., 2018](#)).

Nevertheless, it is still unclear whether or not the local environment of galaxies plays a significant role in the growth of galaxies and their SMBHs. To clarify this, a statistical study of the environment hosting AGN activity is required, and in particular, it is important to determine the occurrence of AGN in PCs.

Studies of high redshift PCs concluded that they exhibit higher fractions of AGN and star-forming galaxies compared to the field, as opposed to overdensities at lower redshifts which have lower fractions than the field (e.g. [Overzier 2016](#), a review; [Martini et al. 2013](#)).

For instance, [Lehmer et al. \(2009, 2013\)](#), [Digby-North et al. \(2010\)](#) and [Krishnan et al. \(2017\)](#), measured AGN fractions in PC of ~ 6 , 3.5 , 20 (or 6 , depending on the method) and 2 times higher than in the field, respectively. Also [Polletta et al. \(2021\)](#) found similar results for AGN fraction ($= 13\% \pm 6\%$) in a PC at $z = 2.16$. Recently, [Macuga et al. \(2019\)](#) found a PC at $z = 2.53$ with an AGN fraction ~ 2 times lower than in the field, indicating a lack of clarity regarding the AGN activity in PCs.

Figure 1.1.3 shows [Macuga et al. \(2019\)](#)'s results, alongside the AGN fraction from the studies of [Lehmer et al. \(2009, 2013\)](#), [Digby-North et al. \(2010\)](#) and [Krishnan et al. \(2017\)](#). In this figure it is possible to see different AGN fractions in protoclusters and field galaxies, as a function of redshift. Mainly, all fractions are higher in PCs at $z > 2$, except for [Macuga et al. 2019](#). Is also important to

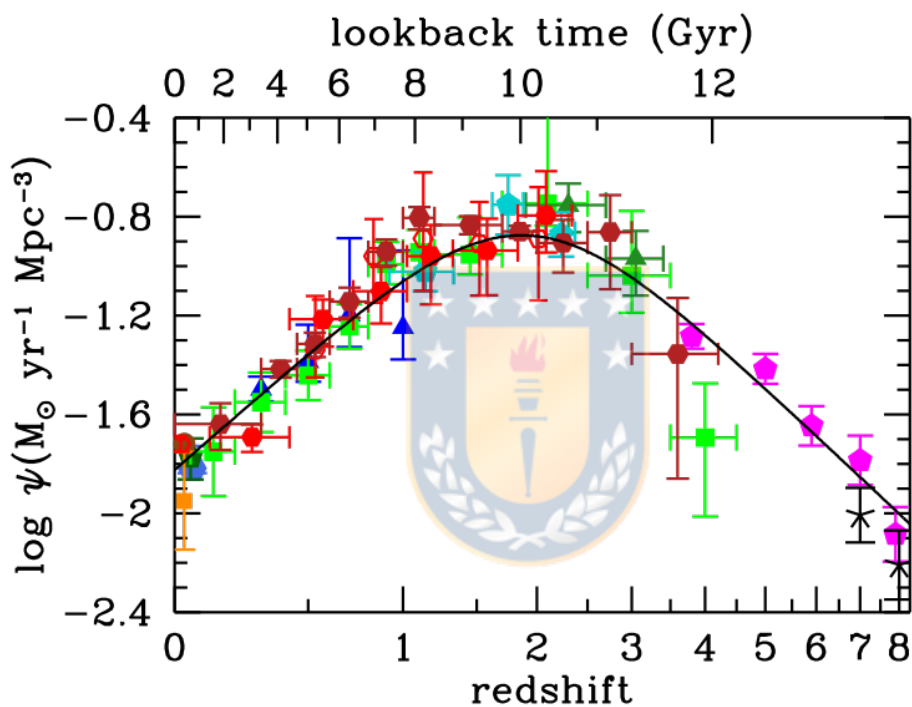


Figure 1.1.2: History of cosmic star formation, derived with FUV+IR rest-frame measurements, from [Madau and Dickinson \(2014\)](#). This figure clearly shows the peak around redshift $z \sim 2 - 3$. Different colors denote different observations, while the black line shows the best fit.

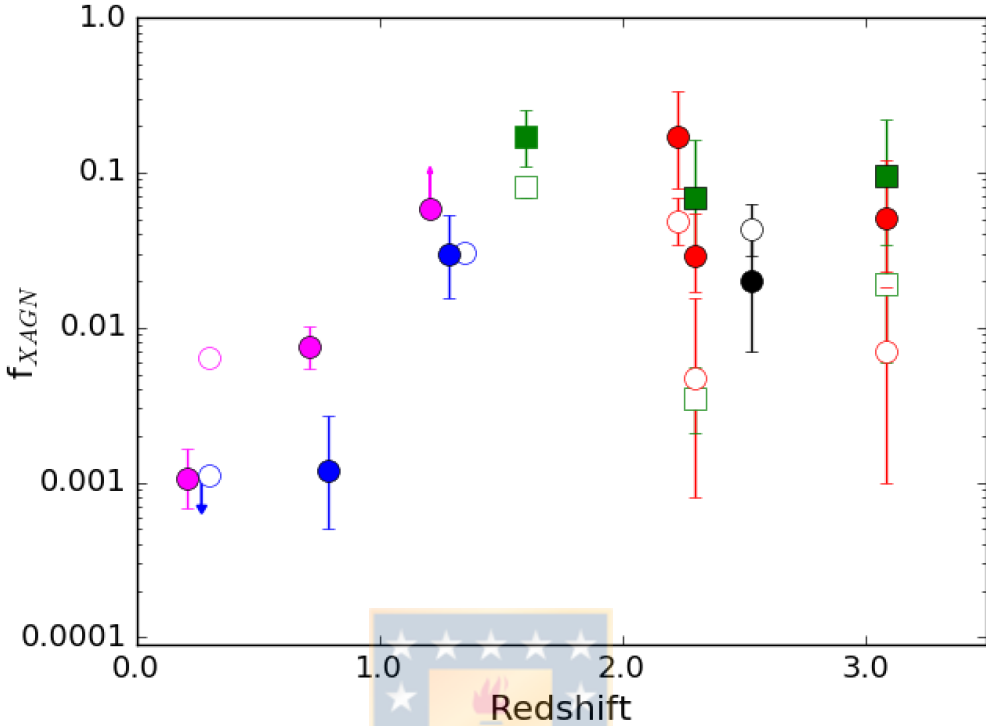


Figure 1.1.3: AGN fractions in protoclusters (filled symbols) and field galaxies (empty symbols), as a function of redshift. Here it is shown how the AGN fraction is lower in PCs for $z < 1$, comparable at $1 < z < 1.5$, and usually higher at $z < 2$, with Macuga et al. 2019 results (black symbols) as an exception. Red symbols are measurements using emission lines, green symbols denote measurements using broad-band colors and purple and blue show averages for large samples of clusters.

note that these AGN fractions were measured with relatively low statistics per sample (see for instance Table 3 from Macuga et al. 2019).

Further, all of these studies showing a larger AGN fraction are based on X-ray selected AGN. This type of selection is biased against highly obscured sources (Hatcher et al., 2021, and references therein). Therefore, to provide a complete picture, other methods must be used to select AGN.

Whether differences in AGN fractions are due to redshift evolution, observational biases of PC selected in different halo masses or evolutionary states, variations in the general and systematic properties of PC depending on how they are selected or just individual PC-to-PC variations remains a crucial open question.

Large samples of PC candidates have been built using large photometric surveys that have mapped significant areas of the sky, and some effort has been made to

characterize these kind of environments (e.g., Chiang et al. 2013; Umehata et al. 2015; Lee et al. 2016; Shimakawa et al. 2018; Miller et al. 2019). Performing a larger census of galaxies, especially AGN, within PCs is crucial to understanding the physical processes involved and determine whether the environment of a forming galaxy cluster at high redshift can actually trigger or drive the growth of SMBHs in its member galaxy population.

1.2 Thesis objective

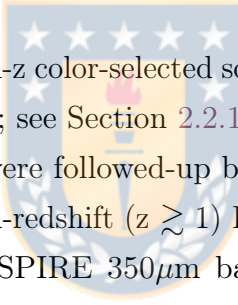
The main goal of this study is to measure the AGN fraction in a large sample of PC candidates. We use the sample of 228 Planck selected PC candidates found in Planck Collaboration et al. 2015 (hereafter Planck XXVII), which itself is drawn from a more general sample of Planck High-redshift candidates (Planck Collaboration et al., 2016). This sample was followed-up by Herschel/SPIRE, and it is biased towards highly-star forming regions. We combined the Planck XXVII catalogue with the data from the Wide-field Infrared Source Explorer (WISE; Wright et al. 2010) AllWISE data release, which has mapped the whole sky. Using WISE sources allows us to use a mid-IR method that selects both obscured and unobscured AGN (Stern et al., 2012). For this we built a classifier that includes both a clustering machine learning algorithm and a W1-W2 colour cut. With the classification of our sources, we were able to estimate AGN fractions in both PC members and field galaxies.

This thesis is organized as follows: in Section 2 we describe our Planck XXVII sample and its WISE counterparts, along with the control sample needed to construct our classifier; in Section 3 we present how we classify AGN sources with our classifier together with estimates of the method uncertainty; in Section 4 we present the measured AGN fractions and our comparison to previous results in the literature; and in Section 6 we discussed our results and present our conclusions.

Chapter 2

Data and Catalogs

2.1 Overview



In this thesis, we study high- z color-selected sources from the [Planck Collaboration et al. 2015](#) (Planck XXVII; see Section 2.2.1). In particular, we use a catalogue of 228 Planck fields that were followed-up by Herschel/SPIRE. These fields are expected to be reliable high-redshift ($z \gtrsim 1$) PC candidates. The sources detected at $> 3\sigma$ in the Herschel/SPIRE $350\mu\text{m}$ band will be referred to as "SPIRE sources".

In order to have a higher resolution photometry than Herschel/SPIRE, we use their WISE counterparts (see Section 2.2.2).

In order to create a classification scheme that selects AGN, we compiled a control sample that includes catalogues of AGN (see Section 2.3.1) and non-AGN sources (see Section 2.3.2).

2.2 Main sample

2.2.1 Planck XXVII

Our main sample consists of the Herschel/SPIRE follow-up observations of 228 Planck sources from [Planck Collaboration et al. \(2015\)](#). These fields, selected as cold sources of the cosmic infrared background (CIB) and from the Planck catalogue of Compact Sources (PCCS), were chosen for follow-up because their

rest-frame far-infrared colours show a peak between the frequency range 353-857 GHz, allowing the selection of ultra luminous infrared galaxies in the redshift range $1 < z < 3$. This sample is thus supposed to be dominated by dusty far infrared galaxies, with high star formation rates.

In this catalogue, an unusually high concentration of bright and compact sources which peak at $350\text{ }\mu\text{m}$ were found, suggesting the presence of highly-star forming PCs, chance line-of-sight projections, and strongly-lensed sources. A few protoclusters have been confirmed in the $1 < z < 3$ range from this sample (Flores-Cacho et al., 2016; Kneissl et al., 2019; Koyama et al., 2021; Polletta et al., 2021, 2022; Lammers et al., 2022; Berman et al., 2022), although Negrello et al. (2017) advocates that most of these structures may be line-of-sight alignments.

Our photometric catalogue for this sample includes the Herschel/SPIRE photometry of 7099 sources at $250\mu\text{m}$, $350\mu\text{m}$ and $500\mu\text{m}$ with angular resolutions (FWHM) of $17''.9$, $24''.2$ and $35''.4$, respectively. The sources in this catalogue are flagged as “in” (“out”) following if the source is in the inner (outer) side of a region defined as the 50% Planck intensity contour at 545 GHz (Planck Collaboration et al., 2015). This region is approximately 5 arcmin across, with Planck angular resolutions (FWHM) of $4.6'$, $4.8'$ and $4.9'$ for the 857, 545 and 353 GHz maps, respectively (Planck Collaboration et al., 2016, Planck XXXIX).

Following the “in” and “out” flag from the Herschel catalogues, we consider the sources flagged as “in” as (proto-)cluster member candidates, while sources flagged as “out” as field galaxy sources. Also, we discarded the Herschel/SPIRE sources that are considered lensed in this study (Cañameras et al., 2015, Dole H., private communication). After removing the lensed sources, we are left with 193 fields and 6904 sources.

In Figure 2.2.1 we show the WISE image of one of the PC candidates as an example. We show the W2 band image for the field PLCK_HZ_G086.1plus61.6, along with the “in” and “out” sources (pink and cyan circles, respectively). The Herschel $500\mu\text{m}$ emission is also shown in yellow contours, showing the difference in resolution between Herschel and WISE. Also, we show the contour at 50% of the peak flux for the Planck image at 545 GHz, that separates the “in” and “out” regions.

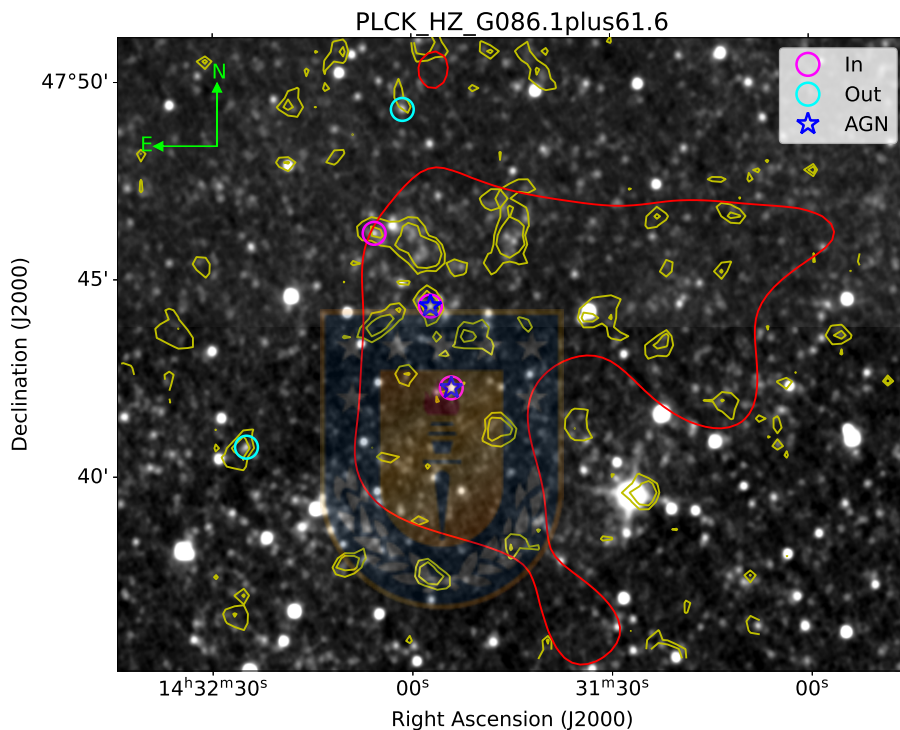


Figure 2.2.1: A 20×16 arcmin 2 WISE observation at $4.6\mu\text{m}$ (W2 band) of one of our PC candidates, PLCK_HZ_G086.1plus61.6, shown as an example. The yellow contours show emission levels at 2σ and 3σ of the Herschel/SPIRE observation at $500\mu\text{m}$, for the same field. The red contour corresponds to the 50% of the peak flux of the respective Planck image at 545 GHz, that separates the “in” and “out” regions. WISE “in” and “out” sources are enclosed by magenta and cyan circles, respectively. The sources enclosed by a blue star were classified as AGN according to our method (see Section 3.1).

2.2.2 Planck XXVII WISE counterparts

The WISE survey is an all-sky mid-IR survey at $3.4\ \mu m$, $4.6\ \mu m$, $12\ \mu m$ and $22\ \mu m$ (the W1, W2, W3 and W4 bands, respectively) with angular resolutions of $6''.1$, $6''.4$, $6''.5$ and $12''.0$. WISE data provide observations with higher resolution compared with those from Herschel/SPIRE with $18''.1$, $25''.2$ and $36''.6$ at $250\ \mu m$, $350\ \mu m$ and $500\ \mu m$, respectively (Griffin et al., 2010). Also, while Herschel probes dust heated by ongoing star formation, WISE W1 and W2 bands probe the stellar emission. Furthermore, WISE observations have been demonstrated to be especially efficient at revealing the presence of an AGN, due to the mid-IR emission of AGN-heated dust (Stern et al., 2012; Mateos et al., 2012; Assef et al., 2013; Hvizing et al., 2022).

We have thus decided to take advantage of the AGN diagnostic power provided by WISE, to assess the presence of AGN activity in the Planck XXVII PC sample, by using the WISE counterparts of our SPIRE sources. Moreover, since we expect PC members to be bright and red sub-mm sources, we are reducing contamination from non members by only selecting WISE sources associated with Herschel sources.

The SPIRE sources were crossmatched with the AllWISE data release¹ (Wright et al., 2010; Mainzer et al., 2011), using the public database from the NASA/IPAC Infrared Science Archive² (IRSA). The match considered only the closest source as a counterpart (avoiding multiple counterparts) in a radius of $9''$, which is half the resolution of the SPIRE's $250\ \mu m$ band. This was a conservative choice to limit wrong associations. We also considered that the WISE sources were photometrically not affected by contamination or artifacts (`cc_flags='0000'`) and that they were point-like (`ext_flg=0`) as expected for high-z sources. We use `w#mpro` Vega magnitudes (where # in the observing band 1, 2, 3 or 4), which is the appropriate magnitude of non-extended sources.

To estimate the completeness of our WISE sample, we look for all the sources in AllWISE within a search radius of 20 arcmin from the Planck's field centres, which is a few times larger than a typical Planck “in” region, obtaining more than 1 million sources. With these sources, we estimate the mean fluxes with

¹Explanatory supplement to the AllWISE data release products in <https://wise2.ipac.caltech.edu/docs/release/allwise/>

²<https://irsa.ipac.caltech.edu/>

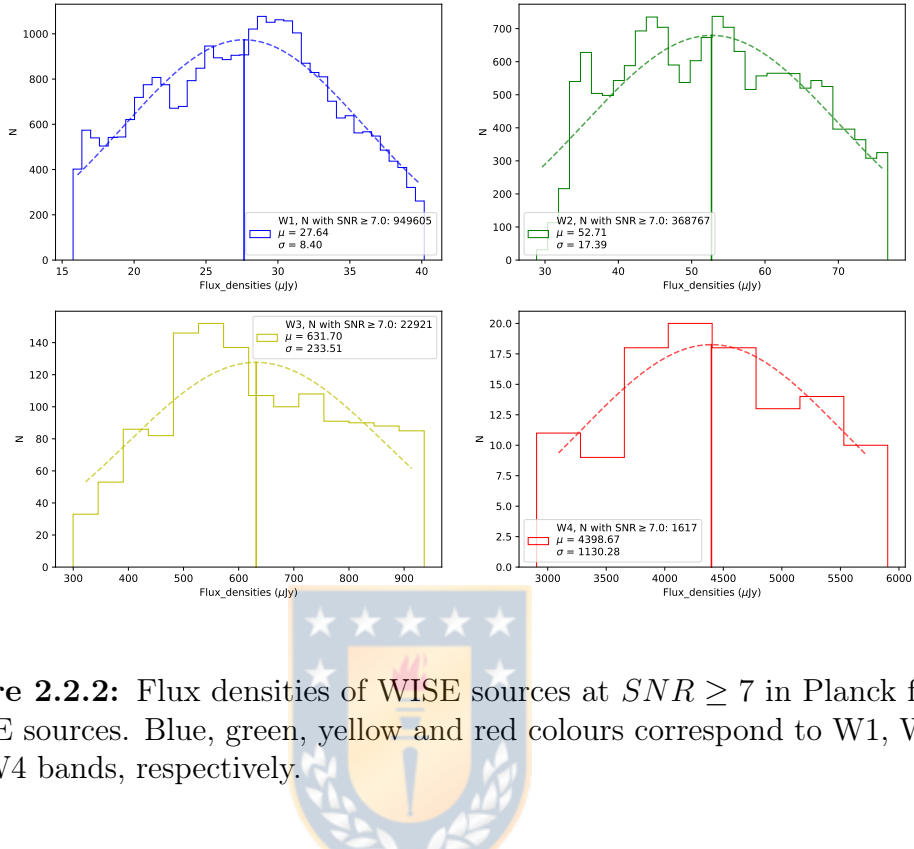


Figure 2.2.2: Flux densities of WISE sources at $SNR \geq 7$ in Planck fields of SPIRE sources. Blue, green, yellow and red colours correspond to W1, W2, W3 and W4 bands, respectively.

different signal-to-noise ratio (SNR) limits for each band and compare them with the AllWISE completeness estimates that were available³.

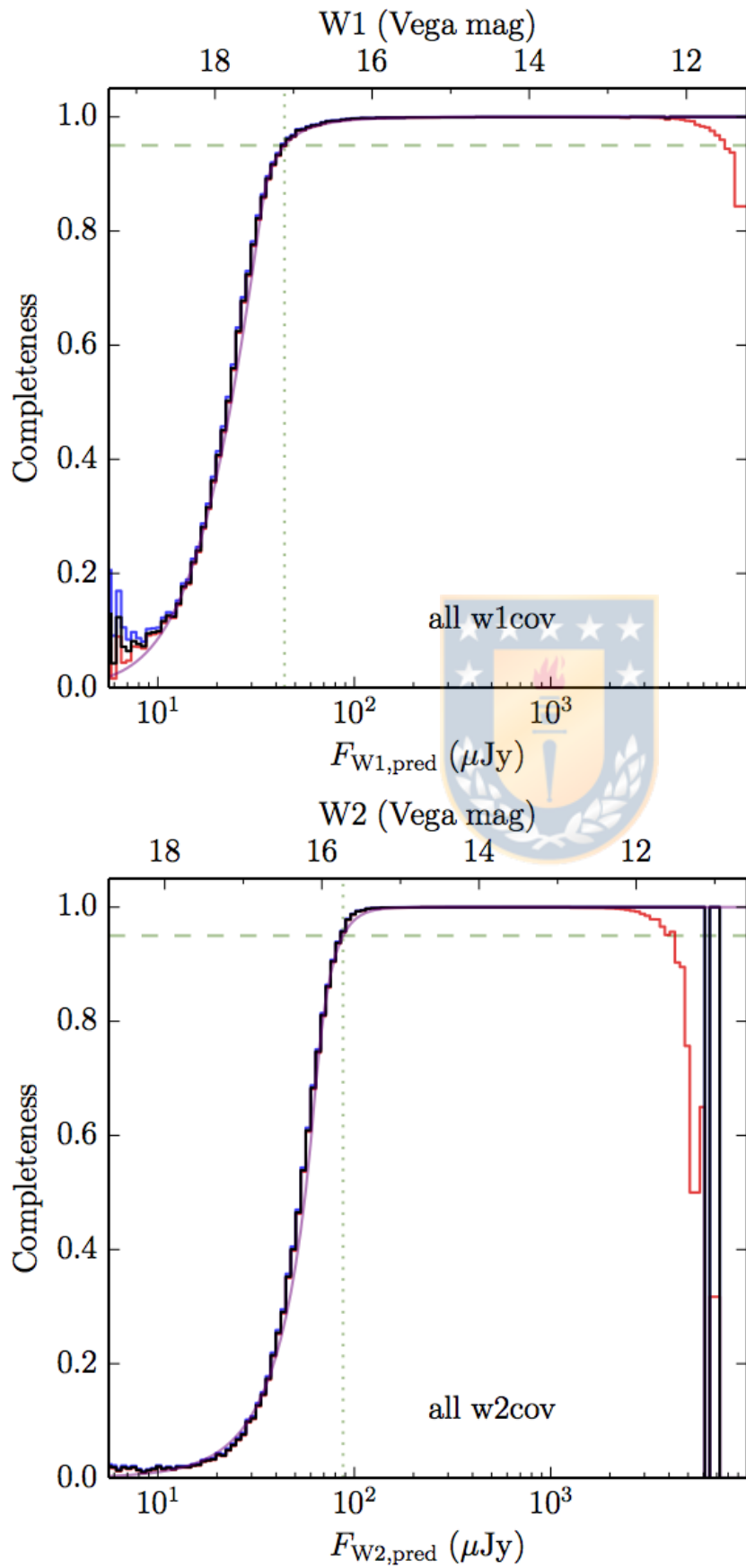
Considering that our Planck XXVII catalogue are secure SPIRE detections, we looked for WISE counterparts with a $SNR \geq 7$, which corresponds to a WISE/AllWISE sample completeness level of at least $\sim 45\%$.

The histograms used to measure the completeness of our WISE counterparts sample are shown in Figure 2.2.2.

The mean of the histograms were then compared to the completeness from a flux density value for each WISE band. This is shown in Figure 2.2.3.

Also, this SNR threshold is consistent with a confident point source detection (Lonsdale et al., 2015). Finally, from our 6904 SPIRE sources we obtain 646 AllWISE counterparts. Out of the total AllWISE sample, 150 are considered PC

³https://wise2.ipac.caltech.edu/docs/release/allwise/expsup/sec2_4a.html#allwisew3w4 for W1 and W2, and https://wise2.ipac.caltech.edu/docs/release/allsky/expsup/sec6_5.html for W3 and W4.



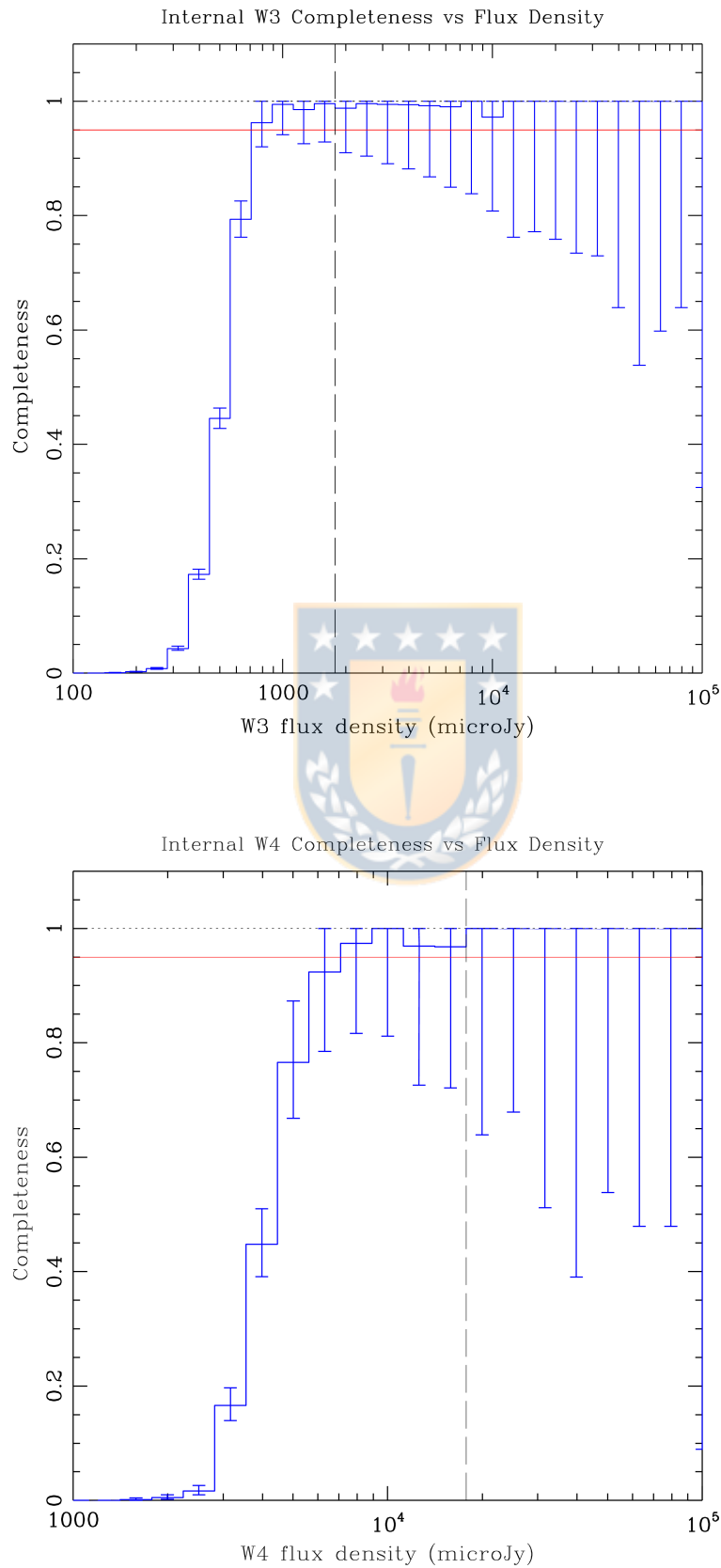


Figure 2.2.3: Completeness of AllWISE catalogue as a function flux density, for the bands W1, W2, W3 and W4.

members (or “in” sources) and 496 are considered field galaxies (or “out” sources). A WISE W1-W2 vs. W2-W3 colour-colour diagram of our AllWISE sources is shown in Figure 2.2.4. Here, we show both the PC members (“in”) and field galaxies (“out”) sources.

2.3 Control Sample

Our control sample comes from a compilation of two catalogues of AGN and two catalogues for SF/non-AGN galaxies. For the AGN subsample, we used the *Veron catalogue of Quasars & AGN, 13th Edition* (VERONCAT; Véron-Cetty and Véron 2010) and the *AGNs in the MIR using AllWISE data* (Secrest et al., 2015) catalogue. For the SF/non-AGN subsample, we use the catalogue of spectroscopic galaxies in WISE+SDSS from Chang et al. (2015) and of star-forming galaxies at $z \sim 1.6$ in the FMOS-COSMOS survey from Kashino et al. (2019).

Since our SPIRE sources are in the (photometric) redshift range $1 < z < 3$, we selected these four mentioned catalogue due to the fact that they have spectroscopic redshifts (z_s) in the same redshift range. The use of spectroscopic redshifts is important to be certain of the redshift range in which we are training our classifier.

The Secrest et al. (2015) and Chang et al. (2015) catalogues already include the magnitudes and colours in the WISE bands. Therefore, we used the WISE colours data available in them.

On the other side, for VERONCAT and Kashino et al. (2019) we did a cross-match with AllWISE, following the same procedure as that for the SPIRE sources, but using a search radius of $6''$, which corresponds to half the best angular resolution of the WISE bands.

2.3.1 AGN

The VERONCAT catalogue contains 168,941 objects of different types of AGN (99,848 sources within $1 \leq z_s \leq 3$). This catalogue is a compilation of all AGN known from the literature (until the VERONCAT’s publication date), including data from the 2dF (Croom et al., 2001, 2004) catalogue, and the data releases (from 1st to 7th; Abazajian et al. 2003, 2004, 2005; Adelman-McCarthy et al. 2006, 2007, 2008; Abazajian et al. 2009) of the Sloan Digital Sky Survey (SDSS; Fan

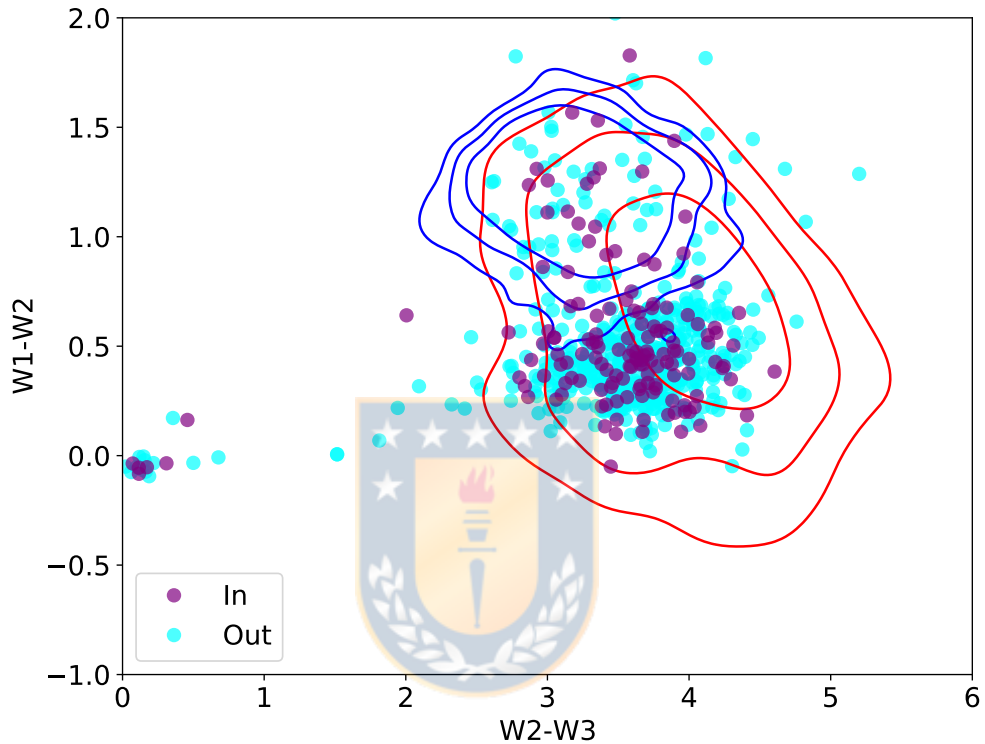


Figure 2.2.4: $W1-W2$ vs. $W2-W3$ colour-colour diagram of the WISE counterparts for the SPIRE sources. Purple and cyan dots show the sources that are “in” and “out” of the Planck 50% intensity region, respectively. The “in” display the same spread in colours as the sources in the “out” region. The over plotted contours show color distribution for our control sample in the 1, 1.5 and 2 σ levels. Blue contours show the distribution for AGN sources, while the red show the non-AGN sources. Our control sample is used to train and test our classifier (see Section 3.1) and includes 614 AGN from the Véron-Cetty and Véron (2010) and the Secrest et al. (2015) catalogues, and 636 SF/non-AGN from the Chang et al. (2015) and Kashino et al. (2019) catalogues (see Section 2.3). We see that most of the SPIRE sources have colours in the same range of the colours from the control sample. The AGN distribution tends to be redder in the $W1-W2$ colour and bluer in the $W2-W3$ colour when compared to SF/non-AGN galaxies.

Table 2.3.1: Summary of our final control sample. For each catalogue we show the type of galaxy selected, the number of sources and the corresponding reference.

Catalogue name	Type	N selected sources	Reference
VERONCAT	AGN	348	Véron-Cetty and Véron (2010)
AGNs in the MIR using AllWISE data	AGN	266	Secrest et al. (2015)
SFR for WISE + SDSS spectroscopic galaxies	SF/non-AGN	120	Chang et al. (2015)
FMOS-COSMOS	SF/non-AGN	516	Kashino et al. (2019)
Total		1250	

et al. 1999) catalogue. The Secrest et al. (2015) catalogue is an all-sky sample that contains more than 1 million sources ($> 66,000$ within $1 \leq z_s \leq 3$), including previously uncatalogued AGN from the AllWISE data release (Wright et al., 2010; Mainzer et al., 2011), using two-colour infrared selection criteria.

2.3.2 SF/non-AGN galaxies

The catalogue from Chang et al. (2015) is a combination of the complete SDSS spectroscopic data with WISE photometry. The full sample contains 858,365 galaxies, however, only 120 sources are in the redshift range of interest and contain WISE colour data available. The catalogue from Kashino et al. (2019) contains 5,484 objects observed over the COSMOS field, with $\sim 30\%$ of them being within $1 \leq z_s \leq 3$. Only 516 sources remained, after cross-matching, with AllWISE photometry.

2.3.3 Balanced Control Sample

The resulting count of sources is a total of 636 SF/non-AGN sources and more than 165,000 AGN.

To have a well statistically balanced sample, we had to reduce our AGN sample by uniformly selecting random sources in order to have a 50% of each type, AGN and non-AGN. Finally we work with a total of 1,250 sources from all catalogue, summarized in Table 2.3.1.

The colour-colour diagram for our final control sample can be seen in the right panel of Figure 2.2.4. Here we distinguish between the AGN and non-AGN

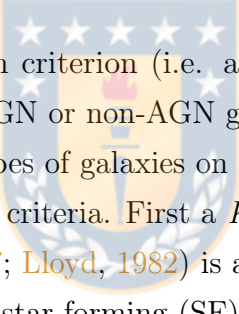
samples. At first glance, no strong separation between AGN and non-AGN can be seen. However, the AGN distribution tends to be redder in the W1-W2 colour and bluer in the W2-W3 colour when compared to SF/non-AGN galaxies.



Chapter 3

Methodology

3.1 AGN classification



We design a colour-colour selection criterion (i.e. a classifier) in order to sort galaxies of our SPIRE sources as AGN or non-AGN galaxies. This is achieved by finding a way of separating both types of galaxies on a W1-W2-W3 colour-colour space. This classifier uses two main criteria. First a *K-means* clustering machine learning algorithm (Macqueen, 1967; Lloyd, 1982) is applied to the WISE colour-colour diagram of known AGN and star-forming (SF)/non-AGN sources (i.e. the control sample). After that, a mid-IR/WISE colour selection criterion is applied. In this case, we use a colour cut of $W1 - W2 \geq 0.721$ (see next subsection). This colour cut is similar to those used in other studies (e.g. Papovich 2008; Stern et al. 2012; Blecha et al. 2018; Lam 2018).

This type of classifier is based on similar studies, that were able to distinguished different types of galaxies, mostly at lower redshifts, in a colour-colour diagram of WISE W1-W2 and W2-W3 colors (Lake et al., 2012; Mingo et al., 2016; Jarrett et al., 2017).

After classifying the WISE counterparts of our SPIRE sources, we estimate the AGN fractions for both the PC members (“in” sources) and field galaxies (“out” sources). The AGN fraction uncertainty is estimated via a Monte Carlo approach.

3.1.1 Building the classifier

Before training our classifier, we subdivide our control sample into a training set, that corresponds to an 85% of the full sample, and a test set, corresponding to the 15% left of the sample. This resulted in 1,062 galaxies for the training set and 188 galaxies for the test set. The percentages that we used to make each sub-sample were decided based on having enough sources to train the classifier, and enough sources that allowed us to evaluate the accuracy of the classifier.

The first part of the classifier consists of using a *k-means* algorithm from the PYTHON package SCIKIT-LEARN (Pedregosa et al., 2011). *K-means* is an unsupervised, machine learning, clustering algorithm. This algorithm subdivides the sample into clusters so that the sum of the squares of the data values in the $W2 - W3$ vs $W1 - W2$ colour-colour space within each cluster is minimized.

The *K-means* module uses the *K-elbow* parameter to decide how many clusters the algorithm will divide the data into. Considering that we want to distinguish between AGN and non-AGN, we set the *K* parameter as $K = 2$, thus dividing the data into two clusters.

Once the algorithm finishes with assigning every data point in the training set to a given cluster, each point gets flagged with either 1 or 0, which means that the source was selected as either an AGN or a non-AGN, respectively. The separation is given by $W1 - W2 = 0.884(W2 - W3) - 2.526$. Since running the *k-means* algorithm alone does not cleanly divide our sample, we added a colour cut into this classifier. This colour cut was defined as the mean minus 3σ of the $W1 - W2$ AGN distribution from our control sample, and corresponds to $W1 - W2 = 0.721$ (see Figure 4.1.1). In summary, we consider a source to be an AGN if its $W1 - W2$ colour agrees with the following:

$$W1 - W2 > \begin{cases} 0.721 & \text{for } W2 - W3 \leq 3.674 \\ 0.884(W2 - W3) - 2.526 & \text{for } W2 - W3 > 3.674 \end{cases} \quad (3.1.1)$$

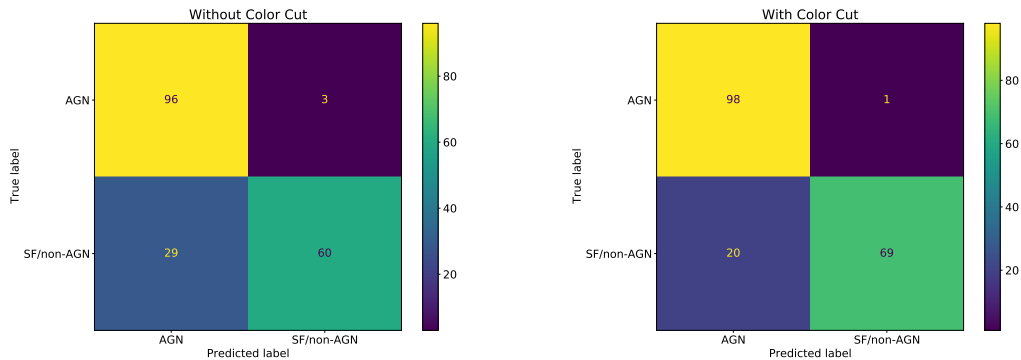


Figure 3.1.1: Confusion matrices of our classification test with a 188 sources test sample. Each matrix shows the number of true positives (top left), false negatives (top right), false positives (bottom left) and true negatives (bottom right). *Left panel:* Confusion matrix for the classifier without adding the colour cut at $W1-W2 = 0.721$. The accuracy of the classification is of 82%, with 97% completeness and 77% reliability. *Right panel:* Confusion Matrix for the classifier, now adding the colour cut at $W1-W2 = 0.721$. The accuracy of the classification using the colour cut increases to an 88.8%, with 99% completeness and 83% reliability.

3.1.2 Testing

We estimate the completeness and reliability of the classifier using the test sample, with a size of 188 sources. We first verify the classification only by considering a *k-means* clustering. This results in a classification of 96 true positives and 60 true negatives, meaning, a completeness of 97% and a reliability of 77%. We then tested these parameters using the combined *k-means* algorithm with the colour cut criterion. This resulted in 69 true negatives and 98 true positives. This essentially means that adding the colour cut improves the completeness and reliability to 99% and 83%, respectively, of our classifier. In Figure 3.1.1 we present the confusion matrices, summarizing these values.

3.1.3 Monte Carlo simulation

To estimate the uncertainty of our method we performed a 10,000-step Monte Carlo simulation. Each step simulates colors in the space $W1-W2$ vs. $W2-W3$, for which we use our classifier and then measure an AGN fraction. In order to construct our simulation, we interpolate the $W1-W2$ and $W2-W3$ colour distributions of the SPIRE sources for both PC members ('in' sources) and field galaxies ('out' sources).

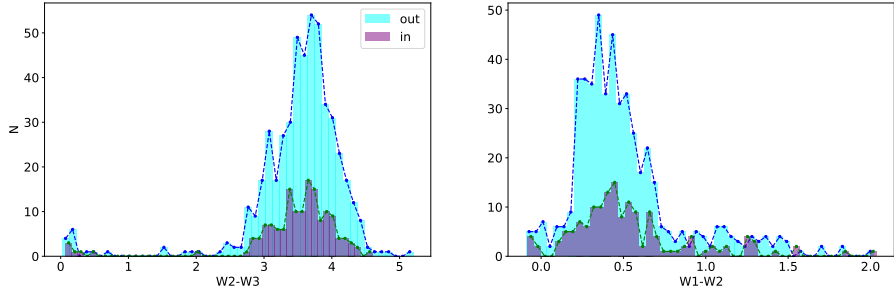


Figure 3.1.2: SPIRE WISE counterparts distributions for the W2-W3 (left panel) and W1-W2 (right panel) colours. Purple and cyan colours represent sources flagged as *in* and *out*, respectively. The green and blue dashed curves show the interpolation to the *in* and *out* distributions. We used these interpolations to generate the simulated data for the Monte Carlo simulation (used to estimate the uncertainty of the classifier).

The SPIRE distributions in each colour and their interpolations are shown in Figure 3.1.2.

Each step simulates the data using random data points generated from the previously mentioned distributions. The W1-W2-W3 colours of one of the artificially generated distributions are shown in Figure 3.1.3.

After that, each simulated data point gets a designation of AGN or non-AGN, using our classifier. Finally, the AGN fractions are measured. This procedure is repeated for PC members and field sources. The Monte Carlo simulation returns a normal distribution for the AGN fractions of the “in” and “out” simulated data, which have a mean and standard deviation of $\mu_{in} = 0.162$ and $\sigma_{in} = 0.03$ for the *in* simulated data, and $\mu_{out} = 0.133$ and $\sigma_{out} = 0.015$ for the *out* simulated data.

The normal distributions resulting from our Monte Carlo simulation are shown in Figure 3.1.4. This figure shows the histogram of the AGN fractions f_{AGN} measured in each of the 10,000 iterations for the “in” sources (left panel) and for the “out” sources (right panel). For each histogram we fitted a gaussian model and found a mean of 0.162 (0.133) and a standard deviation of 0.030 (0.015) for “in” (“out”) sources, respectively. The 1σ standard deviation is what we use as our AGN fraction uncertainties, for “in” and “out” sources.

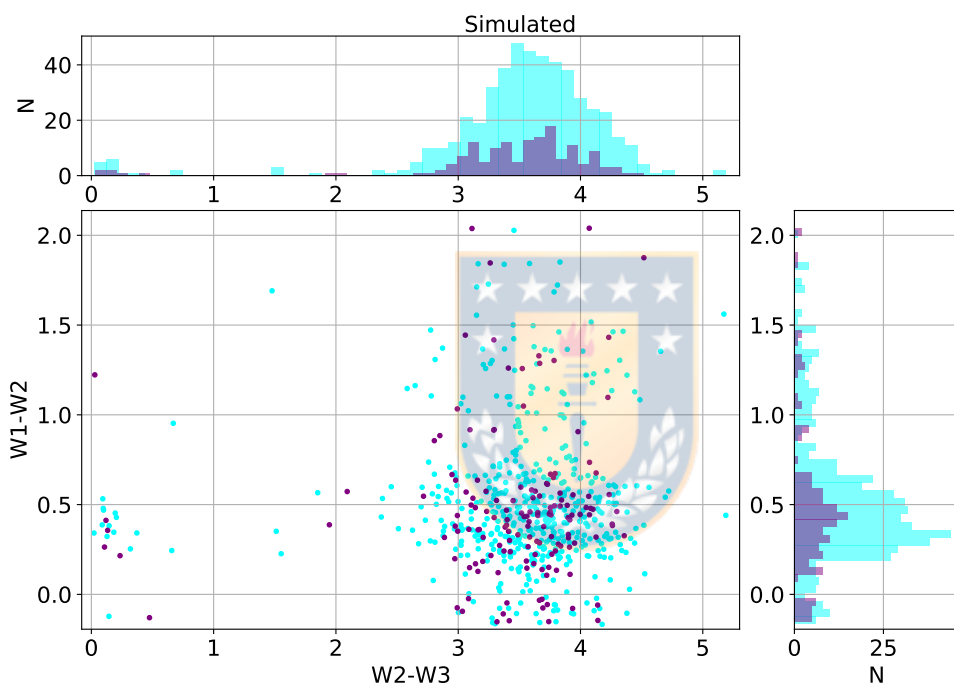


Figure 3.1.3: Example of simulated data for one iteration of the Monte Carlo simulation. The figure shows the colour-colour diagram for $W1-W2$ as a function of $W2-W3$. Purple and cyan colours represent sources flagged as *in* and *out*, respectively. Here we show that the simulated data follow a similar colour-colour distribution than the SPIRE's one, shown in Figures 2.2.4 and 3.1.2.

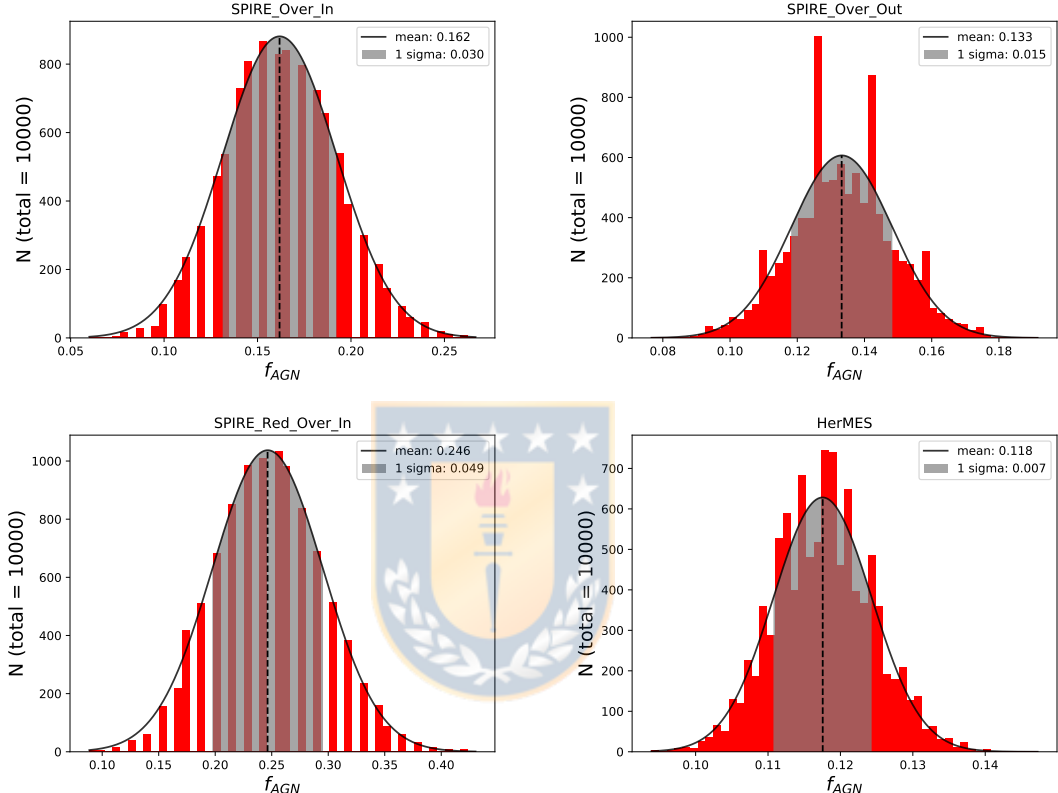


Figure 3.1.4: Resulting normal distributions (red) for the 10,000-step Monte Carlo simulation of the AGN fractions for sources inside (top left panel) and outside (top right panel) PCs. The normal distributions for the Monte Carlo simulations for out redder subsample (bottom left panel) and for the HerMES field sample (bottom right panel) are also shown. The solid black line shows a fitted gaussian model, with its corresponding mean (dashed black line) and standard deviation (shaded gray region). From these normal distribution, we use the $1-\sigma$ standard deviation as our AGN fractions uncertainties. This is, the AGN fraction for “in” sources has an error of 0.030, the AGN fraction for “out” sources has an error of 0.015, the AGN fraction of the redder sample has an error of 0.049 and the AGN fraction of the HerMES sample has en error of 0.007.

Chapter 4

Results

4.1 Classification of the SPIRE sources

We run the classifier with our SPIRE sources and found the following outcome. Out of the full catalogue of 646 sources, we found that 86 are selected as AGN, while 560 are selected as non-AGN sources. In particular, we found that there are 25 AGN that correspond to members of PC candidates and 61 that correspond to sources outside the PC candidates, i.e. field galaxies. When it comes to non-AGN, we found 125 that are also PC members, and 435 sources that correspond to non-PC members. These numbers are summarized in Table 4.1.1.

The final classifier is represented in Figure 4.1.1. In particular, we show the W1-W2 vs W2-W3 colour-colour diagram for our SPIRE sources. The different symbols distinguish between the sources that the classifier selects as AGN or SF/non-AGN. Also, filled and empty symbols differentiate member galaxies of PC from field galaxies, respectively. We also over-plotted the (training) control sample as blue and red contours for AGN and SF/non-AGN objects, respectively, to show the distribution of the galaxies we used to train our *k-means* method.

Table 4.1.1: Classification result of the SPIRE WISE counterparts.

	AGN	non-AGN
In	25	125
Out	61	435
Total	86	560

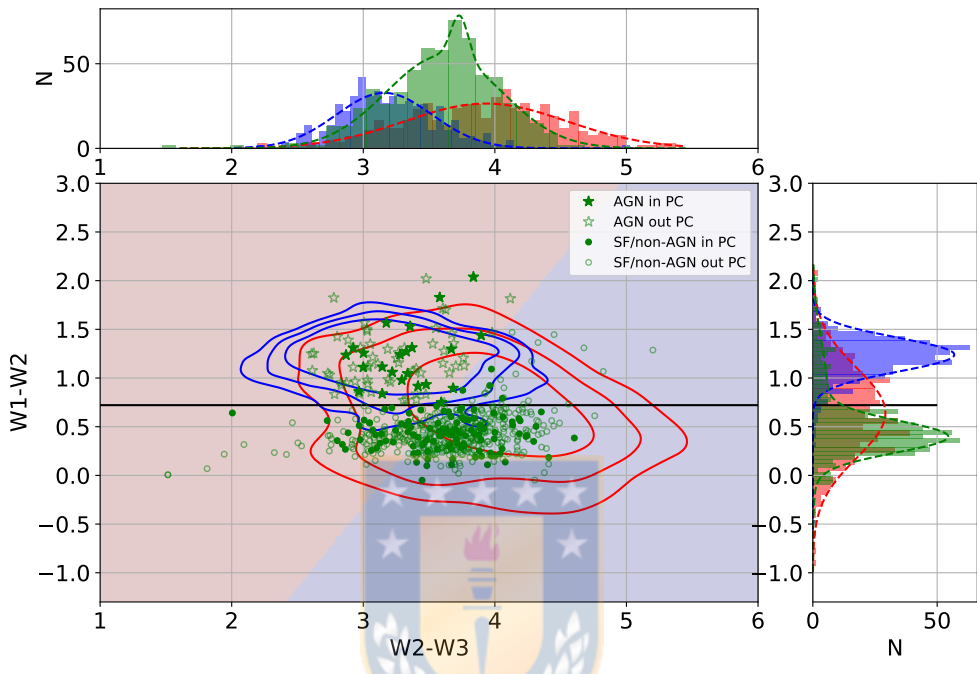


Figure 4.1.1: Classification result for the SPIRE sources (green) in the W1-W2 vs. W2-W3 colour-colour diagram. To consider a source as an AGN, two conditions must be met. The source must be located: (1) above the black horizontal line, which corresponds to a 3σ level threshold for AGN in W1-W2 colour, and (2) over the red background area of the colour-colour diagram, which corresponds to the AGN classification given by the *k-means* separation. Filled (empty) stars represent the sources inside (outside) the PCs that were classified as AGN. Filled (empty) circles are the sources inside (outside) the PCs classified as non-AGN. The blue and red contours show the 1, 1.5 and 2σ levels of the AGN and SF/non-AGN sources in the training data set of our control sample, respectively. This shows that both our main sample and control sample have a similar colour range covered. The upper panel shows the histogram distribution for the W2-W3 colour for the SPIRE sources (green), and for the AGN sources (blue) and the SF/non-AGN sources (red) of the control sample. Similarly, the right side panel shows the histogram of those distributions for the W1-W2 colour, including the 3σ level threshold shown as the solid black line. The different coloured dashed lines show the fitted gaussian model for each distribution.

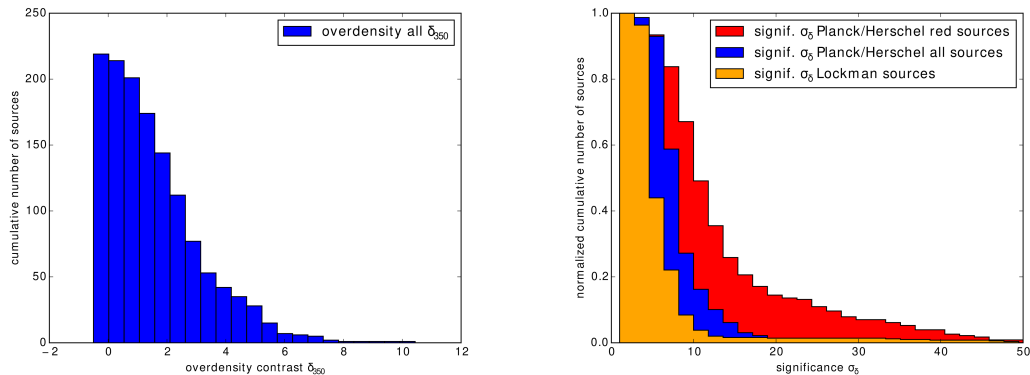


Figure 4.2.1: Figure taken from (Planck Collaboration et al., 2015). Left panel shows the cumulative overdensity for their Planck fields, using $350\mu\text{m}$ SPIRE sources. Right panel shows the normalized cumulative number of sources as a function of the statistical significance in σ from the density maps. This indicates how the red sources have a higher overdensity significance.

4.2 AGN fractions



After the classification of sources in our SPIRE sample, we proceeded to measure the AGN fraction in both the PC candidates and the field. The resulting AGN fraction for PCs is $f_{AGN_{PC}} = 0.167 \pm 0.03$ or 17%. For the field, we found an AGN fraction of $f_{AGN_{Field}} = 0.123 \pm 0.015$ or 12%.

For a better understanding of our results, we also measured the AGN fraction for a SPIRE subsample corresponding to the red SPIRE sources, that fulfill the flux ratio based conditions $S_{350}/S_{250} > 0.7$ and $S_{500}/S_{350} > 0.6$. These red SPIRE sources have an overdensity significance greater than the SPIRE sources (Planck Collaboration et al., 2015). This is shown in Figures 4.2.1 and 4.2.2.

The AGN fraction of these red SPIRE sources is $f_{AGN_{Red}} = 0.283 \pm 0.049$ or 28%.

Hence, at a first glance, we found that the AGN fraction is higher in PC candidates than in the field. However, this difference is not statistically significant considering the uncertainties of our estimates.

To compare the AGN fraction of our SPIRE field ('out') sources, we also measured the AGN fraction of the HerMES (Oliver et al., 2010) "level 5" Lockman-SWIRE field, which has a similar depth to our SPIRE sources (Planck Collaboration et al., 2015). We find that $f_{AGN_{HerMES}} = 0.111 \pm 0.007$ or 11%, which is similar to $f_{AGN_{Field}}$. Figures 4.2.3 and 4.2.4 summarize these fractions.

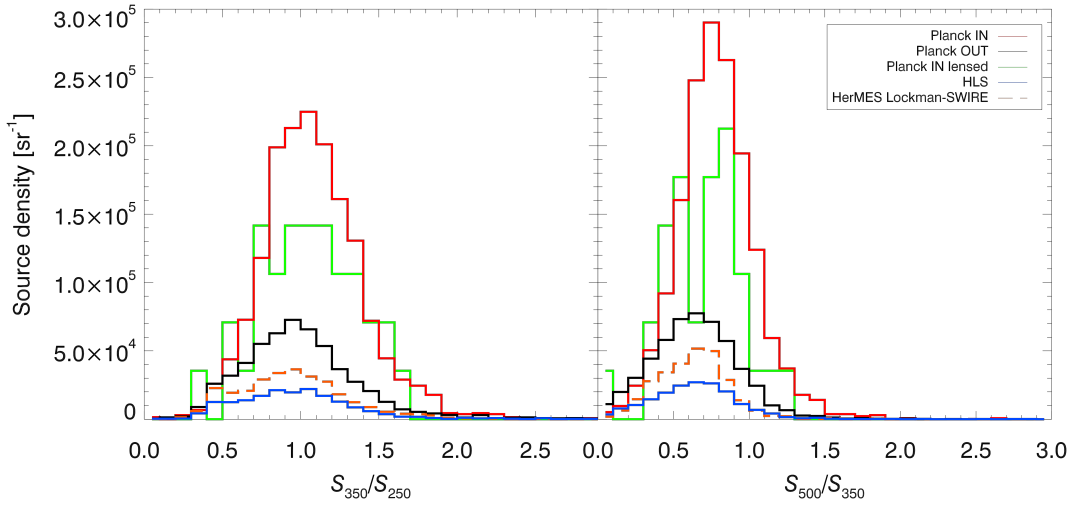


Figure 4.2.2: Figure taken from (Planck Collaboration et al., 2015). This figure shows the source density as a function of the colors S_{350}/S_{250} (left panel) and S_{500}/S_{350} (right panel), for different fields. It is shown how the subsample of "in" sources is higher than other fields.

Since we do not have the exact redshift for each source and only know that these ones are within $1 < z < 3$, we plotted the fractions as a horizontal bar that extends through that redshift range. In order to compare our results, we added AGN fractions from Macuga et al. (2019, and references therein) at a redshift of $z = 2.53$. The figure also includes measurements for different PCs from Lehmer et al. (2009), Digby-North et al. (2010), Lehmer et al. (2013), Polletta et al. (2021) and Krishnan et al. (2017), at redshifts of $z = 3.09, 2.3, 2.23, 2.16$ and 1.6 , respectively. We found similar values of f_{AGN} in PCs to those in Krishnan et al. (2017) and Lehmer et al. (2013), while the others seem lower. It is important to keep in mind that these studies only measured the AGN fraction within one PC, instead of a fraction within a large set of PC members, like in this study.

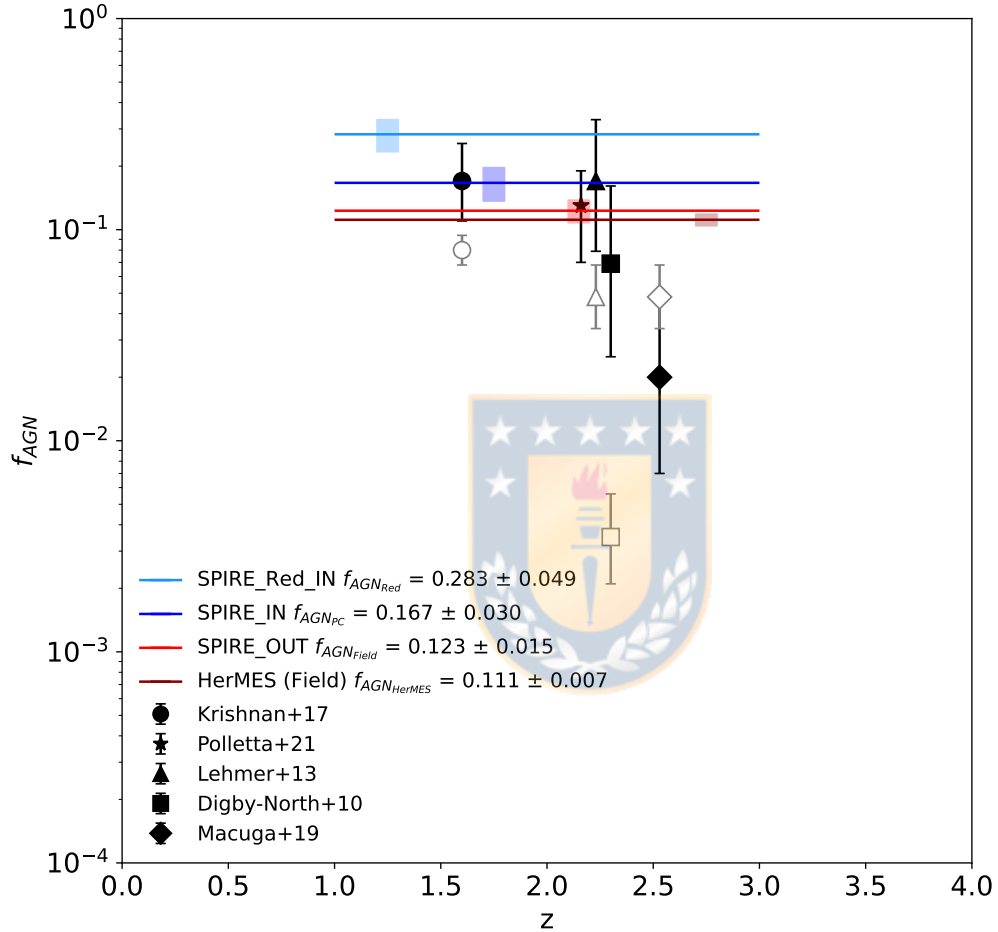


Figure 4.2.3: AGN fractions, f_{AGN} , for the red SPIRE sources (cyan), SPIRE sources that are inside PC (blue), outside PC (red) and HerMES field (dark red) versus redshift. For easier visualization, we show the $1-\sigma$ significance of the AGN fractions as boxes in arbitrary redshift positions. Literature values from Polletta et al. (2021) (black star) and Macuga et al. (2019, and references therein; black circle, triangle, square and diamond) are added as reference for cluster/PC (filled black markers) and field (empty grey markers) galaxies. Here we show that the AGN fraction is, in general, greater in PCs than in the field. See also Figure 4.2.4.

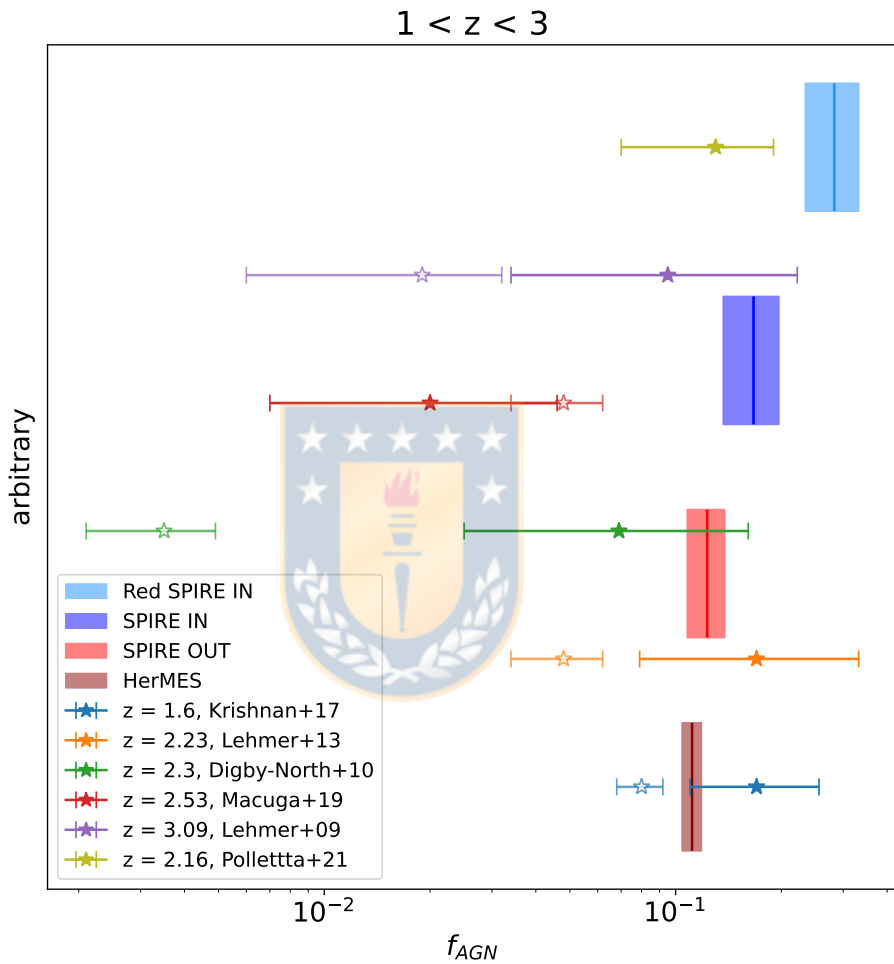


Figure 4.2.4: AGN fractions, f_{AGN} (and $1-\sigma$ significance), for the red SPIRE sources (cyan), SPIRE sources that are inside PC (blue), outside PC (red) and HerMES field (dark red). Literature values from Polletta et al. (2021) and Macuga et al. (2019, and references therein) are added as reference for cluster/PC (filled stars) and field (empty stars) galaxies. The arbitrary y-axis was chosen to better distinguish the difference in the AGN fractions, taking into account their significance. See also Figure 4.2.3.

Chapter 5

Discussion and Conclusions

5.1 Discussion

5.1.1 AGN selection



We expect that training our AGN classifier with a richer data set would return a higher accuracy of classification and better statistical results, since here we were limited by a relatively small sample of star-forming galaxies at high redshift with WISE photometry. Also, considering Stern et al. (2012) and references therein, one could decide on a different colour cut between the range $0.7 \leq W1 - W2 \leq 0.8$, “trading” completeness (bluer colour cut) for reliability (redder colour cut).

Keeping this in mind, plus the fact that our classifier shows an 88.8% of accuracy, we compared our classification method with the one shown in Assef et al. (2018), which also classifies AGN based on a colour condition. Particularly, we compared the number of SPIRE sources selected as AGN, following our criteria versus Assef et al. (2018). This was made by comparing our equation 3.1.1 with equation 4 in Assef et al. (2018). The latter equation includes two outcomes, one for a reliability of 90% and the other for a reliability of 75% (R90 and R75 respectively). We find that the ratio of AGN classified with our method and the Assef’s one, for R90 (R75), is

$$\frac{AGN_{ThisWork}}{AGN_{Assef+18}} = 0.84(0.51).$$

and

$$\frac{AGN_{ThisWork}}{AGN_{Assef+18}} = 0.95(0.73).$$

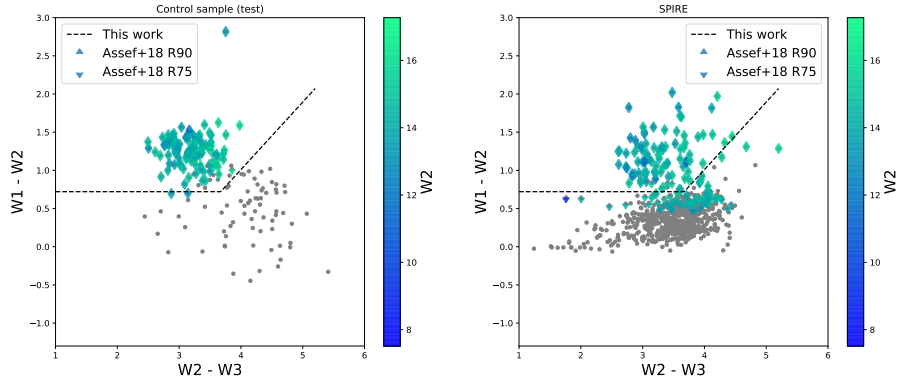


Figure 5.1.1: Comparison of AGN selection criteria between this work and [Assef et al. \(2018\)](#). In the left (right) panel we show the colour-colour distribution of our control (SPIRE) sample (grey dots). The dashed black line shows our AGN selection criterion, while up- and down-pointing triangles correspond to sources selected as AGN following [Assef et al. \(2018\)](#) for R90 and R75, respectively. The AGN selected sources are colour coded for W2 magnitude. The majority of our AGN selected data, 109% from the control sample, 84% from the all SPIRE sample, and 95% from the red SPIRE sources were also selected as AGN following [Assef et al. \(2018\)](#)'s criteria, principally for R90.

for red SPIRE sources. Doing this same analysis with our (test) control sample, we obtain that:

$$\frac{AGN_{ThisWork}}{AGN_{Assef+18}} = 1.09(1.07).$$

However, when comparing the fraction of predicted AGN sources vs. true AGN sources (*True*) we find that:

$$\frac{AGN_{Assef+18}}{True} = 1.08(1.10)$$

for R90(R75), and

$$\frac{AGN_{ThisWork}}{True} = 1.18.$$

This means that the criterion used in [Assef et al. \(2018\)](#) is able to classify all AGN sources as an AGN, but includes an extra 8% (10%) of false positives for R90 (R75), while our method has an extra 18% of false positives. The reason why we obtain slightly more false positives may be due to the mixture of AGN and non-AGN in colour-colour space. In Figure 5.1.1 we show a comparison between [Assef et al. \(2018\)](#)'s and our AGN selection criteria. In Table 5.1.1 we summarized this comparison.

Table 5.1.1: Ratio of AGN classifications following this work and Assef et al. (2018) and the true number of AGN. General comparison between AGN classification from this work and classification from Assef et al. (2018).

ThisWork/Assef+18	R75			R75			R90			R90		
	SPIRE			Red			Test			SPIRE		
	0.51	0.73	1.07	0.84	0.95	1.09						
Assef+18/True	R75						R90					
	1.1						1.08					
ThisWork/True	1.18											

5.1.2 AGN fraction and their implications in protoclusters

The AGN fraction that we find in PCs is not significantly higher than the fraction measured in the field as found by other studies. An important thing to keep in mind is that only a few PC in our sample are confirmed. Therefore, we may have sources that are line-of-sight alignments as suggested by Negrello et al. (2017), instead of members of the overdensities.

We tested if measuring the AGN fraction in a subsample with a higher overdensity significance (i.e. a redder subsample), resulted in a higher AGN fraction. We found a higher AGN fraction than the field by a $\sim 16\%$ (only $\sim 4\%$ higher when comparing the full sample and the field). This could suggest that by selecting this redder sample we were in fact cleaning our sample and removing "line-of-sight alignments", and we would be consistent with higher AGN fraction in PCs.

One of the main limitations of this study is that we are using photometrically selected PC candidates, instead of spectroscopically confirmed structures, due to the paucity of confirmed PCs available. Having a large data set of spectroscopically confirmed overdensities at high redshift would make it possible to better understand the relationship between AGN fractions – and, therefore, the growth history of SMBHs in galaxies – and the evolutionary state of early dense environments.

Nevertheless, WISE-selected AGN appear to be good indicators of overdensities (Jones, 2017), as well as other AGN selections in general (e.g. Noirot et al. 2016, 2018). Plus, follow-up observations from Spitzer/IRAC for some of these PC candidates (Martinache et al., 2018), continue to support the idea that these sources, or at least a good fraction of them, are true members of PC overdensities.

Another possible explanation for finding an AGN fraction not as highly significant in PCs, is that by selecting only sources with a Herschel counterpart, we are only looking at the most star-forming and dustiest members, instead of the full PC population, and the AGN population might not overlap with these.

Finally, the most likely explanation is that many PC members are too faint to be detected by WISE. Further, several PC AGN members may be detected only by W1 and W2 bands, and not in W3. In that case, this would mean that we are looking into the brightest AGN in the structures, which are rare.

In order to test this statement, we looked into how many members of the protocluster PHz G237.01+42.50 (G237) at $z=2.16$ are detected by WISE. This PC has 31 spectroscopically confirmed members (Polletta et al., 2021). Using a crossmatch radius of $6.5''$ (W3 band resolution), out of the 31 sources, we found 5 WISE counterparts. For these counterparts, none of them are detectable in W3 band, i. e. they have, in average, a $\text{SNR} < 1$ in W3 band. In other words, a $\sim 16\%$ of the members were detected in W1 and W2 bands. Similarly, we consider the protocluster MAGAZ3NE J095924+022537 at $z=3.37$ (McConachie et al., 2022). Out of 22 spectroscopically confirmed members, we found 7 sources within $10''$; none detected in W3 band. Thus, a $\sim 31\%$ of the members were detected only in W1 and W2 bands.

Following this analysis, a diagnostic based only on the W1 and W2 may be considered for future work. Alternatively, a stacking analysis on the W3 signal could be done to reveal sources that are too faint to be detected individually.

Also, this analysis could point to the fact that the small difference we found in the AGN fractions for field and PCs may be significant even if statistically is not. Thus, even if we did not find a highly significant difference, we think our results are still hinting to a higher AGN activity in PCs.

5.2 Conclusions

We estimated the AGN fraction in ~ 228 protocluster candidates selected by Planck XXVII and followed-up by Herschel, a representative sample of high redshift ($1 < z < 3$) PC candidate members. This sample provides the photometry for 7099 sources and allowed us to compared the measured AGN fraction of galaxies

inside the overdensities and compared them with field galaxies.

We used the WISE counterparts of these sources, since WISE provides a higher resolution photometry and the possibility of probing the stellar emission. This resulted in a catalogue of 646 counterparts.

In order to select the AGN in our sample, we constructed a classifier based on a mid-IR AllWISE colour-colour selection criterion. This is achieved by combining a $W1-W2 = 0.721$ colour cut, which correspond to the mean minus 3σ of the $W1-W2$ AGN distribution of a control sample made up of AGN and SF/non-AGN catalogue, and a *k-means* clustering algorithm that separates the control sample following the $W1-W2 = 0.884(W2-W3) - 2.526$ relation. Our control sample includes known AGN and non-AGN galaxies that were used to trained our classifier.

Out of the 150 PC members, we found 25 AGN and 125 non-AGN, which corresponds to an AGN fraction of $f_{AGN_{PC}} = 0.167 \pm 0.03$ or 17 %. For the 496 field galaxies, we found 61 AGN and 435 non-AGN, equivalent to an AGN fraction of $f_{AGN_{Field}} = 0.123 \pm 0.015$ or 12 %.

For further study of the AGN fraction in PCs, we also measured the AGN fraction in a “redder” ($S_{350}/S_{250} > 0.7$ and $S_{500}/S_{350} > 0.6$) subsample of our SPIRE sources, which has a higher overdensity significance. We found an AGN fraction of $f_{AGN_{Red}} = 0.283 \pm 0.049$ or 28%. Moreover, to asses our AGN fraction for the field sample, we also measured the AGN fraction in the Lockman-SWIRE field from HerMES. We found an AGN fraction of $f_{AGN_{HerMES}} = 0.111 \pm 0.007$ or 11%.

In terms of AGN activity in PCs, we found that our AGN fraction is not significantly higher in PCs when compared to the field. However, we think that our results hints towards a higher SMBH activity in overdensities, specially since we found a slightly increase in the AGN fraction for the “redder” sample, proportional to the overdensity significance of the sample. For the field, we found that both our sample and the one from HerMES have a similar AGN fraction, thus suggesting that we have a representative field sample.

Our main conclusion is that it is complicated to asses the AGN and SMBH activity in overdensities, particularly at these high redshifts. We believe that it is necessary a combined and complete multi-wavelength study to better understand the role of environment in the evolution of galaxies and their SMBHs. We expect that

new observations from the James Webb Space Telescope will improve these kind of studies by delivering deeper and higher resolution data for galaxies and large scales structures in the redshift interval considered in this work.



Bibliography

Abazajian, K., Adelman-McCarthy, J. K., Agüeros, M. A., Allam, S. S., Anderson, K., Anderson, S. F., Annis, J., Bahcall, N. A., Baldry, I. K., Bastian, S., Berlind, A., Bernardi, M., Blanton, M. R., Bochanski, John J., J., Boroski, W. N., Briggs, J. W., Brinkmann, J., Brunner, R. J., Budavári, T., Carey, L. N., Carliles, S., Castander, F. J., Connolly, A. J., Csabai, I., Doi, M., Dong, F., Eisenstein, D. J., Evans, M. L., Fan, X., Finkbeiner, D. P., Friedman, S. D., Frieman, J. A., Fukugita, M., Gal, R. R., Gillespie, B., Glazebrook, K., Gray, J., Grebel, E. K., Gunn, J. E., Gurbani, V. K., Hall, P. B., Hamabe, M., Harris, F. H., Harris, H. C., Harvanek, M., Heckman, T. M., Hendry, J. S., Hennessy, G. S., Hindsley, R. B., Hogan, C. J., Hogg, D. W., Holmgren, D. J., Ichikawa, S.-i., Ichikawa, T., Ivezić, Ž., Jester, S., Johnston, D. E., Jorgensen, A. M., Kent, S. M., Kleinman, S. J., Knapp, G. R., Kniazev, A. Y., Kron, R. G., Krzesinski, J., Kunszt, P. Z., Kuropatkin, N., Lamb, D. Q., Lampeitl, H., Lee, B. C., Leger, R. F., Li, N., Lin, H., Loh, Y.-S., Long, D. C., Loveday, J., Lupton, R. H., Malik, T., Margon, B., Matsubara, T., McGehee, P. M., McKay, T. A., Meiksin, A., Munn, J. A., Nakajima, R., Nash, T., Neilsen, Eric H., J., Newberg, H. J., Newman, P. R., Nichol, R. C., Nicinski, T., Nieto-Santisteban, M., Nitta, A., Okamura, S., O'Mullane, W., Ostriker, J. P., Owen, R., Padmanabhan, N., Peoples, J., Pier, J. R., Pope, A. C., Quinn, T. R., Richards, G. T., Richmond, M. W., Rix, H.-W., Rockosi, C. M., Schlegel, D. J., Schneider, D. P., Scranton, R., Sekiguchi, M., Seljak, U., Sergey, G., Sesar, B., Sheldon, E., Shimasaku, K., Siegmund, W. A., Silvestri, N. M., Smith, J. A., Smolčić, V., Snedden, S. A., Stebbins, A., Stoughton, C., Strauss, M. A., SubbaRao, M., Szalay, A. S., Szapudi, I., Szkody, P., Szokoly, G. P., Tegmark, M., Teodoro, L., Thakar, A. R., Tremonti, C., Tucker, D. L., Uomoto, A., Vanden Berk, D. E., Vandenberg, J., Vogeley, M. S., Voges, W., Vogt, N. P., Walkowicz, L. M., Wang, S.-i., Weinberg, D. H., West, A. A., White, S. D. M., Wilhite, B. C., Xu, Y., Yanny, B., Yasuda, N., Yip, C.-W., Yocom, D. R., York, D. G., Zehavi, I., Zibetti, S., and Zucker, D. B. (2004). The Second Data Release of the Sloan Digital Sky Survey. , 128(1):502–512.

Abazajian, K., Adelman-McCarthy, J. K., Agüeros, M. A., Allam, S. S., Anderson, K. S. J., Anderson, S. F., Annis, J., Bahcall, N. A., Baldry, I. K., Bastian, S., Berlind, A., Bernardi, M., Blanton, M. R., Bochanski, John J., J., Boroski, W. N., Brewington, H. J., Briggs, J. W., Brinkmann, J., Brunner, R. J., Budavári, T., Carey, L. N., Castander, F. J., Connolly, A. J., Covey, K. R., Csabai, I.,

- Dalcanton, J. J., Doi, M., Dong, F., Eisenstein, D. J., Evans, M. L., Fan, X., Finkbeiner, D. P., Friedman, S. D., Frieman, J. A., Fukugita, M., Gillespie, B., Glazebrook, K., Gray, J., Grebel, E. K., Gunn, J. E., Gurbani, V. K., Hall, P. B., Hamabe, M., Harbeck, D., Harris, F. H., Harris, H. C., Harvanek, M., Hawley, S. L., Hayes, J., Heckman, T. M., Hendry, J. S., Hennessy, G. S., Hindsley, R. B., Hogan, C. J., Hogg, D. W., Holmgren, D. J., Holtzman, J. A., Ichikawa, S.-i., Ichikawa, T., Ivezić, Ž., Jester, S., Johnston, D. E., Jorgensen, A. M., Jurić, M., Kent, S. M., Kleinman, S. J., Knapp, G. R., Kniazev, A. Y., Kron, R. G., Krzesinski, J., Lamb, D. Q., Lampeitl, H., Lee, B. C., Lin, H., Long, D. C., Loveday, J., Lupton, R. H., Mannery, E., Margon, B., Martínez-Delgado, D., Matsubara, T., McGehee, P. M., McKay, T. A., Meiksin, A., Ménard, B., Munn, J. A., Nash, T., Neilsen, Eric H., J., Newberg, H. J., Newman, P. R., Nichol, R. C., Nicinski, T., Nieto-Santisteban, M., Nitta, A., Okamura, S., O'Mullane, W., Owen, R., Padmanabhan, N., Pauls, G., Peoples, J., Pier, J. R., Pope, A. C., Pourbaix, D., Quinn, T. R., Raddick, M. J., Richards, G. T., Richmond, M. W., Rix, H.-W., Rockosi, C. M., Schlegel, D. J., Schneider, D. P., Schroeder, J., Scranton, R., Sekiguchi, M., Sheldon, E., Shimasaku, K., Silvestri, N. M., Smith, J. A., Smolčić, V., Snedden, S. A., Stebbins, A., Stoughton, C., Strauss, M. A., SubbaRao, M., Szalay, A. S., Szapudi, I., Szkody, P., Szokoly, G. P., Tegmark, M., Teodoro, L., Thakar, A. R., Tremonti, C., Tucker, D. L., Uomoto, A., Vanden Berk, D. E., Vandenberg, J., Vogeley, M. S., Voges, W., Vogt, N. P., Walkowicz, L. M., Wang, S.-i., Weinberg, D. H., West, A. A., White, S. D. M., Wilhite, B. C., Xu, Y., Yanny, B., Yasuda, N., Yip, C.-W., Yocom, D. R., York, D. G., Zehavi, I., Zibetti, S., and Zucker, D. B. (2005). The Third Data Release of the Sloan Digital Sky Survey. , 129(3):1755–1759.
- Abazajian, K., Adelman-McCarthy, J. K., Agüeros, M. A., Allam, S. S., Anderson, S. F., Annis, J., Bahcall, N. A., Baldry, I. K., Bastian, S., Berlind, A., Bernardi, M., Blanton, M. R., Blythe, N., Bochanski, John J., J., Boroski, W. N., Brewington, H., Briggs, J. W., Brinkmann, J., Brunner, R. J., Budavári, T., Carey, L. N., Carr, M. A., Castander, F. J., Chiu, K., Collinge, M. J., Connolly, A. J., Covey, K. R., Csabai, I., Dalcanton, J. J., Dodelson, S., Doi, M., Dong, F., Eisenstein, D. J., Evans, M. L., Fan, X., Feldman, P. D., Finkbeiner, D. P., Friedman, S. D., Frieman, J. A., Fukugita, M., Gal, R. R., Gillespie, B., Glazebrook, K., Gonzalez, C. F., Gray, J., Grebel, E. K., Grodnicki, L., Gunn, J. E., Gurbani, V. K., Hall, P. B., Hao, L., Harbeck, D., Harris, F. H., Harris, H. C., Harvanek, M., Hawley, S. L., Heckman, T. M., Helmboldt, J. F., Hendry, J. S., Hennessy, G. S., Hindsley, R. B., Hogg, D. W., Holmgren, D. J., Holtzman, J. A., Homer, L., Hui, L., Ichikawa, S.-i., Ichikawa, T., Inkmann, J. P., Ivezić, Ž., Jester, S., Johnston, D. E., Jordan, B., Jordan, W. P., Jorgensen, A. M., Jurić, M., Kauffmann, G., Kent, S. M., Kleinman, S. J., Knapp, G. R., Kniazev, A. Y., Kron, R. G., Krzesiński, J., Kunszt, P. Z., Kuropatkin, N., Lamb, D. Q., Lampeitl, H., Laubscher, B. E., Lee, B. C., Leger, R. F., Li, N., Lidz, A., Lin, H., Loh, Y.-S., Long, D. C., Loveday, J., Lupton, R. H., Malik, T., Margon, B., McGehee, P. M., McKay, T. A., Meiksin, A., Miknaitis, G. A., Moorthy, B. K., Munn, J. A., Murphy, T., Nakajima, R., Narayanan, V. K., Nash, T.,

Neilsen, Eric H., J., Newberg, H. J., Newman, P. R., Nichol, R. C., Nicinski, T., Nieto-Santisteban, M., Nitta, A., Odenkirchen, M., Okamura, S., Ostriker, J. P., Owen, R., Padmanabhan, N., Peoples, J., Pier, J. R., Pindor, B., Pope, A. C., Quinn, T. R., Rafikov, R. R., Raymond, S. N., Richards, G. T., Richmond, M. W., Rix, H.-W., Rockosi, C. M., Schaye, J., Schlegel, D. J., Schneider, D. P., Schroeder, J., Scranton, R., Sekiguchi, M., Seljak, U., Sergey, G., Sesar, B., Sheldon, E., Shimasaku, K., Siegmund, W. A., Silvestri, N. M., Sinisgalli, A. J., Sirko, E., Smith, J. A., Smolčić, V., Snedden, S. A., Stebbins, A., Steinhardt, C., Stinson, G., Stoughton, C., Strateva, I. V., Strauss, M. A., SubbaRao, M., Szalay, A. S., Szapudi, I., Szkody, P., Tasca, L., Tegmark, M., Thakar, A. R., Tremonti, C., Tucker, D. L., Uomoto, A., Vanden Berk, D. E., Vandenberg, J., Vogeley, M. S., Voges, W., Vogt, N. P., Walkowicz, L. M., Weinberg, D. H., West, A. A., White, S. D. M., Wilhite, B. C., Willman, B., Xu, Y., Yanny, B., Yarger, J., Yasuda, N., Yip, C.-W., Yocom, D. R., York, D. G., Zakamska, N. L., Zehavi, I., Zheng, W., Zibetti, S., and Zucker, D. B. (2003). The First Data Release of the Sloan Digital Sky Survey. , 126(4):2081–2086.

Abazajian, K. N., Adelman-McCarthy, J. K., Agüeros, M. A., Allam, S. S., Allende Prieto, C., An, D., Anderson, K. S. J., Anderson, S. F., Annis, J., Bahcall, N. A., Bailer-Jones, C. A. L., Barentine, J. C., Bassett, B. A., Becker, A. C., Beers, T. C., Bell, E. F., Belokurov, V., Berlind, A. A., Berman, E. F., Bernardi, M., Bickerton, S. J., Bizyaev, D., Blakeslee, J. P., Blanton, M. R., Bochanski, J. J., Boroski, W. N., Brewington, H. J., Brinchmann, J., Brinkmann, J., Brunner, R. J., Budavári, T., Carey, L. N., Carliles, S., Carr, M. A., Castander, F. J., Cinabro, D., Connolly, A. J., Csabai, I., Cunha, C. E., Czarapata, P. C., Davenport, J. R. A., de Haas, E., Dilday, B., Doi, M., Eisenstein, D. J., Evans, M. L., Evans, N. W., Fan, X., Friedman, S. D., Frieman, J. A., Fukugita, M., Gänsicke, B. T., Gates, E., Gillespie, B., Gilmore, G., Gonzalez, B., Gonzalez, C. F., Grebel, E. K., Gunn, J. E., Györy, Z., Hall, P. B., Harding, P., Harris, F. H., Harvanek, M., Hawley, S. L., Hayes, J. J. E., Heckman, T. M., Hendry, J. S., Hennessy, G. S., Hindsley, R. B., Hoblitt, J., Hogan, C. J., Hogg, D. W., Holtzman, J. A., Hyde, J. B., Ichikawa, S.-i., Ichikawa, T., Im, M., Ivezić, Ž., Jester, S., Jiang, L., Johnson, J. A., Jorgensen, A. M., Jurić, M., Kent, S. M., Kessler, R., Kleinman, S. J., Knapp, G. R., Konishi, K., Kron, R. G., Krzesinski, J., Kuropatkin, N., Lampeitl, H., Lebedeva, S., Lee, M. G., Lee, Y. S., French Leger, R., Lépine, S., Li, N., Lima, M., Lin, H., Long, D. C., Loomis, C. P., Loveday, J., Lupton, R. H., Magnier, E., Malanushenko, O., Malanushenko, V., Mandelbaum, R., Margon, B., Marriner, J. P., Martínez-Delgado, D., Matsubara, T., McGehee, P. M., McKay, T. A., Meiksin, A., Morrison, H. L., Mullally, F., Munn, J. A., Murphy, T., Nash, T., Nebot, A., Neilsen, Eric H., J., Newberg, H. J., Newman, P. R., Nichol, R. C., Nicinski, T., Nieto-Santisteban, M., Nitta, A., Okamura, S., Oravetz, D. J., Ostriker, J. P., Owen, R., Padmanabhan, N., Pan, K., Park, C., Pauls, G., Peoples, John, J., Percival, W. J., Pier, J. R., Pope, A. C., Pourbaix, D., Price, P. A., Purger, N., Quinn, T., Raddick, M. J., Re Fiorentin, P., Richards, G. T., Richmond, M. W., Riess, A. G., Rix, H.-W., Rockosi, C. M., Sako, M., Schlegel, D. J.,

- Schneider, D. P., Scholz, R.-D., Schreiber, M. R., Schwone, A. D., Seljak, U., Sesar, B., Sheldon, E., Shimasaku, K., Sibley, V. C., Simmons, A. E., Sivarani, T., Allyn Smith, J., Smith, M. C., Smolčić, V., Snedden, S. A., Stebbins, A., Steinmetz, M., Stoughton, C., Strauss, M. A., SubbaRao, M., Suto, Y., Szalay, A. S., Szapudi, I., Szkody, P., Tanaka, M., Tegmark, M., Teodoro, L. F. A., Thakar, A. R., Tremonti, C. A., Tucker, D. L., Uomoto, A., Vanden Berk, D. E., Vandenberg, J., Vidrih, S., Vogeley, M. S., Voges, W., Vogt, N. P., Wadadekar, Y., Watters, S., Weinberg, D. H., West, A. A., White, S. D. M., Wilhite, B. C., Wonders, A. C., Yanny, B., Yocom, D. R., York, D. G., Zehavi, I., Zibetti, S., and Zucker, D. B. (2009). The Seventh Data Release of the Sloan Digital Sky Survey. , 182(2):543–558.
- Adelman-McCarthy, J. K., Agüeros, M. A., Allam, S. S., Allende Prieto, C., Anderson, K. S. J., Anderson, S. F., Annis, J., Bahcall, N. A., Bailer-Jones, C. A. L., Baldry, I. K., Barentine, J. C., Bassett, B. A., Becker, A. C., Beers, T. C., Bell, E. F., Berlind, A. A., Bernardi, M., Blanton, M. R., Bochanski, J. J., Boroski, W. N., Brinchmann, J., Brinkmann, J., Brunner, R. J., Budavári, T., Carliles, S., Carr, M. A., Castander, F. J., Cinabro, D., Cool, R. J., Covey, K. R., Csabai, I., Cunha, C. E., Davenport, J. R. A., Dilday, B., Doi, M., Eisenstein, D. J., Evans, M. L., Fan, X., Finkbeiner, D. P., Friedman, S. D., Frieman, J. A., Fukugita, M., Gänsicke, B. T., Gates, E., Gillespie, B., Glazebrook, K., Gray, J., Grebel, E. K., Gunn, J. E., Gurbani, V. K., Hall, P. B., Harding, P., Harvanek, M., Hawley, S. L., Hayes, J., Heckman, T. M., Hendry, J. S., Hindsley, R. B., Hirata, C. M., Hogan, C. J., Hogg, D. W., Hyde, J. B., Ichikawa, S.-i., Ivezić, Ž., Jester, S., Johnson, J. A., Jorgensen, A. M., Jurić, M., Kent, S. M., Kessler, R., Kleinman, S. J., Knapp, G. R., Kron, R. G., Krzesinski, J., Kuropatkin, N., Lamb, D. Q., Lampeitl, H., Lebedeva, S., Lee, Y. S., French Leger, R., Lépine, S., Lima, M., Lin, H., Long, D. C., Loomis, C. P., Loveday, J., Lupton, R. H., Malanushenko, O., Malanushenko, V., Mandelbaum, R., Margon, B., Marriner, J. P., Martínez-Delgado, D., Matsubara, T., McGehee, P. M., McKay, T. A., Meiksin, A., Morrison, H. L., Munn, J. A., Nakajima, R., Neilsen, Eric H., J., Newberg, H. J., Nichol, R. C., Nicinski, T., Nieto-Santisteban, M., Nitta, A., Okamura, S., Owen, R., Oyaizu, H., Padmanabhan, N., Pan, K., Park, C., Peoples, John, J., Pier, J. R., Pope, A. C., Purger, N., Raddick, M. J., Re Fiorentin, P., Richards, G. T., Richmond, M. W., Riess, A. G., Rix, H.-W., Rockosi, C. M., Sako, M., Schlegel, D. J., Schneider, D. P., Schreiber, M. R., Schwone, A. D., Seljak, U., Sesar, B., Sheldon, E., Shimasaku, K., Sivarani, T., Allyn Smith, J., Snedden, S. A., Steinmetz, M., Strauss, M. A., SubbaRao, M., Suto, Y., Szalay, A. S., Szapudi, I., Szkody, P., Tegmark, M., Thakar, A. R., Tremonti, C. A., Tucker, D. L., Uomoto, A., Vanden Berk, D. E., Vandenberg, J., Vidrih, S., Vogeley, M. S., Voges, W., Vogt, N. P., Wadadekar, Y., Weinberg, D. H., West, A. A., White, S. D. M., Wilhite, B. C., Yanny, B., Yocom, D. R., York, D. G., Zehavi, I., and Zucker, D. B. (2008). The Sixth Data Release of the Sloan Digital Sky Survey. , 175(2):297–313.

Adelman-McCarthy, J. K., Agüeros, M. A., Allam, S. S., Anderson, K. S. J.,

Anderson, S. F., Annis, J., Bahcall, N. A., Bailer-Jones, C. A. L., Baldry, I. K., Barentine, J. C., Beers, T. C., Belokurov, V., Berlind, A., Bernardi, M., Blanton, M. R., Bochanski, J. J., Boroski, W. N., Bramich, D. M., Brewington, H. J., Brinchmann, J., Brinkmann, J., Brunner, R. J., Budavári, T., Carey, L. N., Carliles, S., Carr, M. A., Castander, F. J., Connolly, A. J., Cool, R. J., Cunha, C. E., Csabai, I., Dalcanton, J. J., Doi, M., Eisenstein, D. J., Evans, M. L., Evans, N. W., Fan, X., Finkbeiner, D. P., Friedman, S. D., Frieman, J. A., Fukugita, M., Gillespie, B., Gilmore, G., Glazebrook, K., Gray, J., Grebel, E. K., Gunn, J. E., de Haas, E., Hall, P. B., Harvanek, M., Hawley, S. L., Hayes, J., Heckman, T. M., Hendry, J. S., Hennessy, G. S., Hindsley, R. B., Hirata, C. M., Hogan, C. J., Hogg, D. W., Holtzman, J. A., Ichikawa, S.-i., Ichikawa, T., Ivezić, Ž., Jester, S., Johnston, D. E., Jorgensen, A. M., Jurić, M., Kauffmann, G., Kent, S. M., Kleinman, S. J., Knapp, G. R., Kniazev, A. Y., Kron, R. G., Krzesinski, J., Kuropatkin, N., Lamb, D. Q., Lampeitl, H., Lee, B. C., Leger, R. F., Lima, M., Lin, H., Long, D. C., Loveday, J., Lupton, R. H., Mandelbaum, R., Margon, B., Martínez-Delgado, D., Matsubara, T., McGehee, P. M., McKay, T. A., Meiksin, A., Munn, J. A., Nakajima, R., Nash, T., Neilsen, Eric H., J., Newberg, H. J., Nichol, R. C., Nieto-Santisteban, M., Nitta, A., Oyaizu, H., Okamura, S., Ostriker, J. P., Padmanabhan, N., Park, C., Peoples, John, J., Pier, J. R., Pope, A. C., Pourbaix, D., Quinn, T. R., Raddick, M. J., Re Fiorentin, P., Richards, G. T., Richmond, M. W., Rix, H.-W., Rockosi, C. M., Schlegel, D. J., Schneider, D. P., Scranton, R., Seljak, U., Sheldon, E., Shimasaku, K., Silvestri, N. M., Smith, J. A., Smolčić, V., Snedden, S. A., Stebbins, A., Stoughton, C., Strauss, M. A., SubbaRao, M., Suto, Y., Szalay, A. S., Szapudi, I., Szkody, P., Tegmark, M., Thakar, A. R., Tremonti, C. A., Tucker, D. L., Uomoto, A., Vanden Berk, D. E., Vandenberg, J., Vidrih, S., Vogeley, M. S., Voges, W., Vogt, N. P., Weinberg, D. H., West, A. A., White, S. D. M., Wilhite, B., Yanny, B., Yocom, D. R., York, D. G., Zehavi, I., Zibetti, S., and Zucker, D. B. (2007). The Fifth Data Release of the Sloan Digital Sky Survey. , 172(2):634–644.

Adelman-McCarthy, J. K., Agüeros, M. A., Allam, S. S., Anderson, K. S. J., Anderson, S. F., Annis, J., Bahcall, N. A., Baldry, I. K., Barentine, J. C., Berlind, A., Bernardi, M., Blanton, M. R., Boroski, W. N., Brewington, H. J., Brinchmann, J., Brinkmann, J., Brunner, R. J., Budavári, T., Carey, L. N., Carr, M. A., Castander, F. J., Connolly, A. J., Csabai, I., Czarapata, P. C., Dalcanton, J. J., Doi, M., Dong, F., Eisenstein, D. J., Evans, M. L., Fan, X., Finkbeiner, D. P., Friedman, S. D., Frieman, J. A., Fukugita, M., Gillespie, B., Glazebrook, K., Gray, J., Grebel, E. K., Gunn, J. E., Gurbani, V. K., de Haas, E., Hall, P. B., Harris, F. H., Harvanek, M., Hawley, S. L., Hayes, J., Hendry, J. S., Hennessy, G. S., Hindsley, R. B., Hirata, C. M., Hogan, C. J., Hogg, D. W., Holmgren, D. J., Holtzman, J. A., Ichikawa, S.-i., Ivezić, Ž., Jester, S., Johnston, D. E., Jorgensen, A. M., Jurić, M., Kent, S. M., Kleinman, S. J., Knapp, G. R., Kniazev, A. Y., Kron, R. G., Krzesinski, J., Kuropatkin, N., Lamb, D. Q., Lampeitl, H., Lee, B. C., Leger, R. F., Lin, H., Long, D. C., Loveday, J., Lupton, R. H., Margon, B., Martínez-Delgado, D., Mandelbaum,

- R., Matsubara, T., McGehee, P. M., McKay, T. A., Meiksin, A., Munn, J. A., Nakajima, R., Nash, T., Neilsen, Eric H., J., Newberg, H. J., Newman, P. R., Nichol, R. C., Nicinski, T., Nieto-Santisteban, M., Nitta, A., O'Mullane, W., Okamura, S., Owen, R., Padmanabhan, N., Pauls, G., Peoples, John, J., Pier, J. R., Pope, A. C., Pourbaix, D., Quinn, T. R., Richards, G. T., Richmond, M. W., Rockosi, C. M., Schlegel, D. J., Schneider, D. P., Schroeder, J., Scranton, R., Seljak, U., Sheldon, E., Shimasaku, K., Smith, J. A., Smolčić, V., Snedden, S. A., Stoughton, C., Strauss, M. A., SubbaRao, M., Szalay, A. S., Szapudi, I., Szkody, P., Tegmark, M., Thakar, A. R., Tucker, D. L., Uomoto, A., Vanden Berk, D. E., Vandenberg, J., Vogeley, M. S., Voges, W., Vogt, N. P., Walkowicz, L. M., Weinberg, D. H., West, A. A., White, S. D. M., Xu, Y., Yanny, B., Yocom, D. R., York, D. G., Zehavi, I., Zibetti, S., and Zucker, D. B. (2006). The Fourth Data Release of the Sloan Digital Sky Survey. , 162(1):38–48.
- Assef, R. J., Stern, D., Kochanek, C. S., Blain, A. W., Brodwin, M., Brown, M. J. I., Donoso, E., Eisenhardt, P. R. M., Jannuzi, B. T., Jarrett, T. H., Stanford, S. A., Tsai, C. W., Wu, J., and Yan, L. (2013). Mid-infrared Selection of Active Galactic Nuclei with the Wide-field Infrared Survey Explorer. II. Properties of WISE-selected Active Galactic Nuclei in the NDWFS Boötes Field. , 772(1):26.
- Assef, R. J., Stern, D., Noirot, G., Jun, H. D., Cutri, R. M., and Eisenhardt, P. R. M. (2018). The WISE AGN Catalog. , 234(2):23.
- Berman, D. A., Yun, M. S., Harrington, K. C., Kamieneski, P., Lowenthal, J., Frye, B. L., Wang, Q. D., Wilson, G. W., Artxaga, I., Chavez, M., Cybulski, R., De la Luz, V., Erickson, N., Ferrusca, D., Hughes, D. H., Montaña, A., Narayanan, G., Sánchez-Argüelles, D., Schloerb, F. P., Souccar, K., Terlevich, E., Terlevich, R., and Zavala, J. A. (2022). PASSAGES: the Large Millimeter Telescope and ALMA observations of extremely luminous high-redshift galaxies identified by the Planck. , 515(3):3911–3937.
- Blecha, L., Snyder, G. F., Satyapal, S., and Ellison, S. L. (2018). The power of infrared AGN selection in mergers: a theoretical study. , 478(3):3056–3071.
- Bongiorno, A., Zamorani, G., Gavignaud, I., Marano, B., Paltani, S., Mathez, G., Møller, P., Picat, J. P., Cirasuolo, M., Lamareille, F., Bottini, D., Garilli, B., Le Brun, V., Le Fèvre, O., Maccagni, D., Scaramella, R., Scoveggio, M., Tresse, L., Vettolani, G., Zanichelli, A., Adami, C., Arnouts, S., Bardelli, S., Bolzonella, M., Cappi, A., Charlot, S., Ciliegi, P., Contini, T., Foucaud, S., Franzetti, P., Guzzo, L., Ilbert, O., Iovino, A., McCracken, H. J., Marinoni, C., Mazure, A., Meneux, B., Merighi, R., Pellò, R., Pollo, A., Pozzetti, L., Radovich, M., Zucca, E., Hatziminaoglou, E., Polletta, M., Bondi, M., Brinchmann, J., Cucciati, O., de la Torre, S., Gregorini, L., Mellier, Y., Merluzzi, P., Temporin, S., Vergani, D., and Walcher, C. J. (2007). The VVDS type-1 AGN sample: the faint end of the luminosity function. , 472(2):443–454.

- Cañameras, R., Nesvadba, N. P. H., Guery, D., McKenzie, T., König, S., Petitpas, G., Dole, H., Frye, B., Flores-Cacho, I., Montier, L., Negrello, M., Beelen, A., Boone, F., Dicken, D., Lagache, G., Le Floc'h, E., Altieri, B., Béthermin, M., Chary, R., de Zotti, G., Giard, M., Kneissl, R., Krips, M., Malhotra, S., Martinache, C., Omont, A., Pointecouteau, E., Puget, J. L., Scott, D., Soucail, G., Valtchanov, I., Welikala, N., and Yan, L. (2015). Planck's dusty GEMS: The brightest gravitationally lensed galaxies discovered with the Planck all-sky survey. , 581:A105.
- Chang, Y.-Y., van der Wel, A., da Cunha, E., and Rix, H.-W. (2015). Stellar Masses and Star Formation Rates for 1M Galaxies from SDSS+WISE. , 219(1):8.
- Chiang, Y.-K., Overzier, R., and Gebhardt, K. (2013). Ancient Light from Young Cosmic Cities: Physical and Observational Signatures of Galaxy Proto-clusters. , 779(2):127.
- Croom, S. M., Smith, R. J., Boyle, B. J., Shanks, T., Loaring, N. S., Miller, L., and Lewis, I. J. (2001). The 2dF QSO Redshift Survey - V. The 10k catalogue. , 322(4):L29–L36.
- Croom, S. M., Smith, R. J., Boyle, B. J., Shanks, T., Miller, L., Outram, P. J., and Loaring, N. S. (2004). The 2dF QSO Redshift Survey - XII. The spectroscopic catalogue and luminosity function. , 349(4):1397–1418.
- Demarco, R., Gobat, R., Rosati, P., Lidman, C., Rettura, A., Nonino, M., van der Wel, A., Jee, M. J., Blakeslee, J. P., Ford, H. C., and Postman, M. (2010). Star Formation Histories in a Cluster Environment at $z \sim 0.84$. , 725(1):1252–1276.
- Díaz-Santos, T., Assef, R. J., Blain, A. W., Aravena, M., Stern, D., Tsai, C. W., Eisenhardt, P., Wu, J., Jun, H. D., Dibert, K., Inami, H., Lansbury, G., and Leclercq, F. (2018). The multiple merger assembly of a hyperluminous obscured quasar at redshift 4.6. *Science*, 362(6418):1034–1036.
- Digby-North, J. A., Nandra, K., Laird, E. S., Steidel, C. C., Georgakakis, A., Bogosavljević, M., Erb, D. K., Shapley, A. E., Reddy, N. A., and Aird, J. (2010). Excess AGN activity in the $z = 2.30$ Protocluster in HS 1700+64. , 407(2):846–853.
- Fan, X., Strauss, M. A., Schneider, D. P., Gunn, J. E., Lupton, R. H., Yanny, B., Anderson, S. F., Anderson, John E., J., Annis, J., Bahcall, N. A., Bakken, J. A., Bastian, S., Berman, E., Boroski, W. N., Briegel, C., Briggs, J. W., Brinkmann, J., Carr, M. A., Colestock, P. L., Connolly, A. J., Crocker, J. H., Csabai, I., Czarapata, P. C., Davis, J. E., Doi, M., Elms, B. R., Evans, M. L., Federwitz, G. R., Frieman, J. A., Fukugita, M., Gurbani, V. K., Harris, F. H., Heckman, T. M., Hennessy, G. S., Hindsley, R. B., Holmgren, D. J., Hull, C., Ichikawa, S.-I., Ichikawa, T., Ivezić, Ž. E., Kent, S., Knapp, G. R., Kron, R. G., Lamb, D. Q., Leger, R. F., Limmongkol, S., Lindenmeyer, C., Long, D. C., Loveday, J., MacKinnon, B., Mannery, E. J., Mantsch, P. M., Margon, B., McKay, T. A., Munn, J. A., Nash, T., Newberg, H. J., Nichol, R. C., Nicinski, T., Okamura,

- S., Ostriker, J. P., Owen, R., Pauls, A. G., Peoples, J., Pet travick, D., Pier, J. R., Pordes, R., Prosapio, A., Rechenmacher, R., Richards, G. T., Richmond, M. W., Rivetta, C. H., Rockosi, C. M., Sandford, D., Sergey, G., Sekiguchi, M., Shimasaku, K., Siegmund, W. A., Smith, J. A., Stoughton, C., Szalay, A. S., Szokoly, G. P., Tucker, D. L., Vogeley, M. S., Waddell, P., Wang, S.-I., Weinberg, D. H., Yasuda, N., and York, D. G. (1999). High-Redshift Quasars Found in Sloan Digital Sky Survey Commissioning Data. , 118(1):1–13.
- Fanidakis, N., Baugh, C. M., Benson, A. J., Bower, R. G., Cole, S., Done, C., Frenk, C. S., Hickox, R. C., Lacey, C., and Del P. Lagos, C. (2012). The evolution of active galactic nuclei across cosmic time: what is downsizing? , 419(4):2797–2820.
- Flores-Cacho, I., Pierini, D., Soucail, G., Montier, L., Dole, H., Pointecouteau, E., Pelló, R., Le Floc'h, E., Nesvadba, N., Lagache, G., Guery, D., and Cañameras, R. (2016). Multi-wavelength characterisation of $z \sim 2$ clustered, dusty star-forming galaxies discovered by Planck. , 585:A54.
- Griffin, M. J., Abergel, A., Abreu, A., Ade, P. A. R., André, P., Augueres, J. L., Babbedge, T., Bae, Y., Baillie, T., Baluteau, J. P., Barlow, M. J., Bendo, G., Benielli, D., Bock, J. J., Bonhomme, P., Brisbin, D., Brockley-Blatt, C., Caldwell, M., Cara, C., Castro-Rodriguez, N., Cerulli, R., Chanial, P., Chen, S., Clark, E., Clements, D. L., Clerc, L., Coker, J., Communal, D., Conversi, L., Cox, P., Crumb, D., Cunningham, C., Daly, F., Davis, G. R., de Antoni, P., Delderfield, J., Devin, N., di Giorgio, A., Diduschuns, I., Dohlen, K., Donati, M., Dowell, A., Dowell, C. D., Duband, L., Dumaye, L., Emery, R. J., Ferlet, M., Ferrand, D., Fontignie, J., Fox, M., Franceschini, A., Frerking, M., Fulton, T., Garcia, J., Gastaud, R., Gear, W. K., Glenn, J., Goizel, A., Griffin, D. K., Grundy, T., Guest, S., Guillemet, L., Hargrave, P. C., Harwit, M., Hastings, P., Hatziminaoglou, E., Herman, M., Hinde, B., Hristov, V., Huang, M., Imhof, P., Isaak, K. J., Israelsson, U., Ivison, R. J., Jennings, D., Kiernan, B., King, K. J., Lange, A. E., Latter, W., Laurent, G., Laurent, P., Leeks, S. J., Lellouch, E., Levenson, L., Li, B., Li, J., Lilienthal, J., Lim, T., Liu, S. J., Lu, N., Madden, S., Mainetti, G., Marliani, P., McKay, D., Mercier, K., Molinari, S., Morris, H., Moseley, H., Mulder, J., Mur, M., Naylor, D. A., Nguyen, H., O'Halloran, B., Oliver, S., Olofsson, G., Olofsson, H. G., Orfei, R., Page, M. J., Pain, I., Panuzzo, P., Papageorgiou, A., Parks, G., Parr-Burman, P., Pearce, A., Pearson, C., Pérez-Fournon, I., Pinsard, F., Pisano, G., Podosek, J., Pohlen, M., Polehampton, E. T., Pouliquen, D., Rigopoulou, D., Rizzo, D., Roseboom, I. G., Roussel, H., Rowan-Robinson, M., Rownd, B., Saraceno, P., Sauvage, M., Savage, R., Savini, G., Sawyer, E., Scharmberg, C., Schmitt, D., Schneider, N., Schulz, B., Schwartz, A., Shafer, R., Shupe, D. L., Sibthorpe, B., Sidher, S., Smith, A., Smith, A. J., Smith, D., Spencer, L., Stobie, B., Sudiwala, R., Sukhatme, K., Surace, C., Stevens, J. A., Swinyard, B. M., Trichas, M., Tourette, T., Triou, H., Tseng, S., Tucker, C., Turner, A., Vaccari, M., Valtchanov, I., Vigroux, L., Virique, E., Voellmer, G., Walker, H., Ward, R., Waskett, T., Weilert, M., Wesson, R., White, G. J., Whitehouse, N., Wilson, C. D., Winter,

- B., Woodcraft, A. L., Wright, G. S., Xu, C. K., Zavagno, A., Zemcov, M., Zhang, L., and Zonca, E. (2010). The Herschel-SPIRE instrument and its in-flight performance. , 518:L3.
- Hasinger, G., Miyaji, T., and Schmidt, M. (2005). Luminosity-dependent evolution of soft X-ray selected AGN. New Chandra and XMM-Newton surveys. , 441(2):417–434.
- Hatcher, C., Kirkpatrick, A., Fornasini, F., Civano, F., Lambrides, E., Kocesvski, D., Carroll, C. M., Giavalisco, M., Hickox, R., and Ji, Z. (2021). Where Do Obscured AGN Fit in a Galaxy’s Timeline? , 162(2):65.
- Hviding, R. E., Hainline, K. N., Rieke, M., Juneau, S., Lyu, J., and Pucha, R. (2022). A New Infrared Criterion for Selecting Active Galactic Nuclei to Lower Luminosities. , 163(5):224.
- Jarrett, T. H., Cluver, M. E., Magoulas, C., Bilicki, M., Alpaslan, M., Bland-Hawthorn, J., Brough, S., Brown, M. J. I., Croom, S., Driver, S., Holwerda, B. W., Hopkins, A. M., Loveday, J., Norberg, P., Peacock, J. A., Popescu, C. C., Sadler, E. M., Taylor, E. N., Tuffs, R. J., and Wang, L. (2017). Galaxy and Mass Assembly (GAMA): Exploring the WISE Web in G12. , 836(2):182.
- Jones, S. F. (2017). The Overdense Environments of WISE-selected, ultra-luminous, high-redshift AGN in the submillimetre. *Frontiers in Astronomy and Space Sciences*, 4:51.
- Kashino, D., Silverman, J. D., Sanders, D., Kartaltepe, J., Daddi, E., Renzini, A., Rodighiero, G., Puglisi, A., Valentino, F., Juneau, S., Arimoto, N., Nagao, T., Ilbert, O., Le Fèvre, O., and Koekemoer, A. M. (2019). The FMOS-COSMOS Survey of Star-forming Galaxies at $z \sim 1.6$. VI. Redshift and Emission-line Catalog and Basic Properties of Star-forming Galaxies. , 241(1):10.
- Kneissl, R., Polletta, M. d. C., Martinache, C., Hill, R., Clarenc, B., Dole, H. A., Nesvadba, N. P. H., Scott, D., Béthermin, M., Frye, B., Giard, M., Lagache, G., and Montier, L. (2019). Using ALMA to resolve the nature of the early star-forming large-scale structure PLCK G073.4-57.5. , 625:A96.
- Koyama, Y., Polletta, M. d. C., Tanaka, I., Kodama, T., Dole, H., Soucail, G., Frye, B., Lehnert, M., and Scudegger, M. (2021). A Planck-selected dusty protocluster at $z = 2.16$ associated with a strong overdensity of massive H α -emitting galaxies. , 503(1):L1–L5.
- Krishnan, C., Hatch, N. A., Almaini, O., Kocevski, D., Cooke, E. A., Hartley, W. G., Hasinger, G., Maltby, D. T., Muldrew, S. I., and Simpson, C. (2017). Enhancement of AGN in a protocluster at $z = 1.6$. , 470(2):2170–2178.
- Lake, S. E., Wright, E. L., Petty, S., Assef, R. J., Jarrett, T. H., Stanford, S. A., Stern, D., and Tsai, C. W. (2012). Optical Spectroscopic Survey of High-latitude WISE-selected Sources. , 143(1):7.

- Lam, A. C. (2018). *Multiwavelength Analyses of Mid-Infrared Selected Active Galactic Nuclei*. PhD thesis, University of California, Los Angeles.
- Lammers, C., Hill, R., Lim, S., Scott, D., Cañameras, R., and Dole, H. (2022). Candidate high-redshift protoclusters and lensed galaxies in the Planck list of high-z sources overlapping with Herschel-SPIRE imaging. , 514(4):5004–5023.
- Lee, K.-G., Hennawi, J. F., White, M., Prochaska, J. X., Font-Ribera, A., Schlegel, D. J., Rich, R. M., Suzuki, N., Stark, C. W., Le Fèvre, O., Nugent, P. E., Salvato, M., and Zamorani, G. (2016). Shadow of a Colossus: A $z = 2.44$ Galaxy Protocluster Detected in 3D Ly α Forest Tomographic Mapping of the COSMOS Field. , 817(2):160.
- Lehmer, B. D., Alexander, D. M., Geach, J. E., Smail, I., Basu-Zych, A., Bauer, F. E., Chapman, S. C., Matsuda, Y., Scharf, C. A., Volonteri, M., and Yamada, T. (2009). The Chandra Deep Protocluster Survey: Evidence for an Enhancement of AGN Activity in the SSA22 Protocluster at $z = 3.09$. , 691(1):687–695.
- Lehmer, B. D., Lucy, A. B., Alexander, D. M., Best, P. N., Geach, J. E., Harrison, C. M., Hornschemeier, A. E., Matsuda, Y., Mullaney, J. R., Smail, I., Sobral, D., and Swinbank, A. M. (2013). Concurrent Supermassive Black Hole and Galaxy Growth: Linking Environment and Nuclear Activity in $z = 2.23$ H α Emitters. , 765(2):87.
- Lloyd, S. (1982). Least squares quantization in pcm. *IEEE Transactions on Information Theory*, 28(2):129–137.
- Lonsdale, C. J., Lacy, M., Kimball, A. E., Blain, A., Whittle, M., Wilkes, B., Stern, D., Condon, J., Kim, M., Assef, R. J., Tsai, C. W., Efstathiou, A., Jones, S., Eisenhardt, P., Bridge, C., Wu, J., Lonsdale, C. J., Jones, K., Jarrett, T., and Smith, R. (2015). Radio Jet Feedback and Star Formation in Heavily Obscured, Hyperluminous Quasars at Redshifts $\sim 0.5\text{--}3$. I. ALMA Observations. , 813(1):45.
- Macqueen, J. (1967). Some methods for classification and analysis of multivariate observations. In *In 5-th Berkeley Symposium on Mathematical Statistics and Probability*, pages 281–297.
- Macuga, M., Martini, P., Miller, E. D., Brodwin, M., Hayashi, M., Kodama, T., Koyama, Y., Overzier, R. A., Shimakawa, R., Tadaki, K.-i., and Tanaka, I. (2019). The Fraction of Active Galactic Nuclei in the USS 1558-003 Protocluster at $z = 2.53$. , 874(1):54.
- Madau, P. and Dickinson, M. (2014). Cosmic star-formation history. *Annual Review of Astronomy and Astrophysics*, 52(1):415–486.
- Mainzer, A., Bauer, J., Grav, T., Masiero, J., Cutri, R. M., Dailey, J., Eisenhardt, P., McMillan, R. S., Wright, E., Walker, R., Jedicke, R., Spahr, T., Tholen, D., Alles, R., Beck, R., Brandenburg, H., Conrow, T., Evans, T., Fowler, J., Jarrett,

- T., Marsh, K., Masci, F., McCallon, H., Wheelock, S., Wittman, M., Wyatt, P., DeBaun, E., Elliott, G., Elsbury, D., Gautier, T., I., Gomillion, S., Leisawitz, D., Maleszewski, C., Micheli, M., and Wilkins, A. (2011). Preliminary Results from NEOWISE: An Enhancement to the Wide-field Infrared Survey Explorer for Solar System Science. , 731(1):53.
- Martinache, C., Rettura, A., Dole, H., Lehnert, M., Frye, B., Altieri, B., Beelen, A., Béthermin, M., Le Floc'h, E., Giard, M., Hurier, G., Lagache, G., Montier, L., Omont, A., Pointecouteau, E., Polletta, M., Puget, J. L., Scott, D., Soucail, G., and Welikala, N. (2018). Spitzer Planck Herschel Infrared Cluster (SPHerIC) survey: Candidate galaxy clusters at $1.3 < z < 3$ selected by high star-formation rate. , 620:A198.
- Martini, P., Miller, E. D., Brodwin, M., Stanford, S. A., Gonzalez, A. H., Bautz, M., Hickox, R. C., Stern, D., Eisenhardt, P. R., Galametz, A., Norman, D., Jannuzzi, B. T., Dey, A., Murray, S., Jones, C., and Brown, M. J. I. (2013). The Cluster and Field Galaxy Active Galactic Nucleus Fraction at $z = 1\text{--}1.5$: Evidence for a Reversal of the Local Anticorrelation between Environment and AGN Fraction. , 768(1):1.
- Mateos, S., Alonso-Herrero, A., Carrera, F. J., Blain, A., Watson, M. G., Barcons, X., Braito, V., Severgnini, P., Donley, J. L., and Stern, D. (2012). Using the Bright Ultrahard XMM-Newton survey to define an IR selection of luminous AGN based on WISE colours. , 426(4):3271–3281.
- McConachie, I., Wilson, G., Forrest, B., Marsan, Z. C., Muzzin, A., Cooper, M. C., Annunziatella, M., Marchesini, D., Chan, J. C. C., Gomez, P., Abdullah, M. H., Saracco, P., and Nantais, J. (2022). Spectroscopic Confirmation of a Protocluster at $z = 3.37$ with a High Fraction of Quiescent Galaxies. , 926(1):37.
- Miller, J. S. A., Bolton, J. S., and Hatch, N. (2019). Searching for the shadows of giants: characterizing protoclusters with line of sight Lyman- α absorption. , 489(4):5381–5397.
- Mingo, B., Watson, M. G., Rosen, S. R., Hardcastle, M. J., Ruiz, A., Blain, A., Carrera, F. J., Mateos, S., Pineau, F. X., and Stewart, G. C. (2016). The MIXR sample: AGN activity versus star formation across the cross-correlation of WISE, 3XMM, and FIRST/NVSS. , 462(3):2631–2667.
- Muldrew, S. I., Hatch, N. A., and Cooke, E. A. (2015). What are protoclusters? - Defining high-redshift galaxy clusters and protoclusters. , 452(3):2528–2539.
- Negrello, M., Gonzalez-Nuevo, J., De Zotti, G., Bonato, M., Cai, Z. Y., Clements, D., Danese, L., Dole, H., Greenslade, J., Lapi, A., and Montier, L. (2017). On the statistics of proto-cluster candidates detected in the Planck all-sky survey. , 470(2):2253–2261.
- Noirot, G., Stern, D., Mei, S., Wylezalek, D., Cooke, E. A., De Breuck, C., Galametz, A., Hatch, N. A., Vernet, J., Brodwin, M., Eisenhardt, P., Gonzalez, A. H., Jarvis, M., Rettura, A., Seymour, N., and Stanford, S. A. (2018). HST

- Grism Confirmation of 16 Structures at $1.4 < z < 2.8$ from the Clusters Around Radio-Loud AGN (CARLA) Survey. , 859(1):38.
- Noirot, G., Vernet, J., De Breuck, C., Wylezalek, D., Galametz, A., Stern, D., Mei, S., Brodwin, M., Cooke, E. A., Gonzalez, A. H., Hatch, N. A., Rettura, A., and Stanford, S. A. (2016). HST Grism Confirmation of Two $z \sim 2$ Structures from the Clusters around Radio-loud AGN (CARLA) Survey. , 830(2):90.
- Oliver, S. J., Wang, L., Smith, A. J., Altieri, B., Amblard, A., Arumugam, V., Auld, R., Aussel, H., Babbedge, T., Blain, A., Bock, J., Boselli, A., Buat, V., Burgarella, D., Castro-Rodríguez, N., Cava, A., Chanial, P., Clements, D. L., Conley, A., Conversi, L., Cooray, A., Dowell, C. D., Dwek, E., Eales, S., Elbaz, D., Fox, M., Franceschini, A., Gear, W., Glenn, J., Griffin, M., Halpern, M., Hatziminaoglou, E., Ibar, E., Isaak, K., Ivison, R. J., Lagache, G., Levenson, L., Lu, N., Madden, S., Maffei, B., Mainetti, G., Marchetti, L., Mitchell-Wynne, K., Mortier, A. M. J., Nguyen, H. T., O'Halloran, B., Omont, A., Page, M. J., Panuzzo, P., Papageorgiou, A., Pearson, C. P., Pérez-Fournon, I., Pohlen, M., Rawlings, J. I., Raymond, G., Rigopoulou, D., Rizzo, D., Roseboom, I. G., Rowan-Robinson, M., Sánchez Portal, M., Savage, R., Schulz, B., Scott, D., Seymour, N., Shupe, D. L., Stevens, J. A., Symeonidis, M., Trichas, M., Tugwell, K. E., Vaccari, M., Valiante, E., Valtchanov, I., Vieira, J. D., Vigroux, L., Ward, R., Wright, G., Xu, C. K., and Zemcov, M. (2010). HerMES: SPIRE galaxy number counts at 250, 350, and 500 μm . , 518:L21.
- Oort, J. H. (1983). Superclusters. , 21:373–428.
- Overzier, R. A. (2016). The realm of the galaxy protoclusters. A review. , 24(1):14.
- Papovich, C. (2008). The Angular Clustering of Distant Galaxy Clusters. , 676(1):206–217.
- Pedregosa, F., Varoquaux, G., Gramfort, A., Michel, V., Thirion, B., Grisel, O., Blondel, M., Prettenhofer, P., Weiss, R., Dubourg, V., Vanderplas, J., Passos, A., Cournapeau, D., Brucher, M., Perrot, M., and Duchesnay, E. (2011). Scikit-learn: Machine learning in python. *J. Mach. Learn. Res.*, 12(null):2825–2830.
- Piconcelli, E., Vignali, C., Bianchi, S., Zappacosta, L., Fritz, J., Lanzuisi, G., Miniutti, G., Bongiorno, A., Feruglio, C., Fiore, F., and Maiolino, R. (2015). The hidden quasar nucleus of a WISE-selected, hyperluminous, dust-obscured galaxy at $z \sim 2.3$. , 574:L9.
- Planck Collaboration, Ade, P. A. R., Aghanim, N., Arnaud, M., Aumont, J., Baccigalupi, C., Banday, A. J., Barreiro, R. B., Bartolo, N., Battaner, E., Benabed, K., Benoit-Lévy, A., Bernard, J. P., Bersanelli, M., Bielewicz, P., Bonaldi, A., Bonavera, L., Bond, J. R., Borrill, J., Bouchet, F. R., Boulanger, F., Burigana, C., Butler, R. C., Calabrese, E., Catalano, A., Chiang, H. C., Christensen, P. R., Clements, D. L., Colombo, L. P. L., Couchot, F., Coulais, A., Crill, B. P., Curto, A., Cuttaia, F., Danese, L., Davies, R. D., Davis, R. J., de Bernardis, P., de Rosa, A., de Zotti, G., Delabrouille, J., Dickinson, C., Diego,

J. M., Dole, H., Doré, O., Douspis, M., Ducout, A., Dupac, X., Elsner, F., Enßlin, T. A., Eriksen, H. K., Falgarone, E., Finelli, F., Flores-Cacho, I., Frailis, M., Fraisse, A. A., Franceschi, E., Galeotta, S., Galli, S., Ganga, K., Giard, M., Giraud-Héraud, Y., Gjerløw, E., González-Nuevo, J., Górski, K. M., Gregorio, A., Gruppuso, A., Gudmundsson, J. E., Hansen, F. K., Harrison, D. L., Helou, G., Hernández-Monteagudo, C., Herranz, D., Hildebrandt, S. R., Hivon, E., Hobson, M., Hornstrup, A., Hovest, W., Huffenberger, K. M., Hurier, G., Jaffe, A. H., Jaffe, T. R., Keihänen, E., Keskitalo, R., Kisner, T. S., Kneissl, R., Knoche, J., Kunz, M., Kurki-Suonio, H., Lagache, G., Lamarre, J. M., Lasenby, A., Lattanzi, M., Lawrence, C. R., Leonardi, R., Levrier, F., Liguori, M., Lilje, P. B., Linden-Vørnle, M., López-Caniego, M., Lubin, P. M., Macías-Pérez, J. F., Maffei, B., Maggio, G., Maino, D., Mandolesi, N., Mangilli, A., Maris, M., Martin, P. G., Martínez-González, E., Masi, S., Matarrese, S., Melchiorri, A., Mennella, A., Migliaccio, M., Mitra, S., Miville-Deschénes, M. A., Moneti, A., Montier, L., Morgante, G., Mortlock, D., Munshi, D., Murphy, J. A., Nati, F., Natoli, P., Nesvadba, N. P. H., Noviello, F., Novikov, D., Novikov, I., Oxborow, C. A., Pagano, L., Pajot, F., Paoletti, D., Partridge, B., Pasian, F., Pearson, T. J., Perdereau, O., Perotto, L., Pettorino, V., Piacentini, F., Piat, M., Plaszczynski, S., Pointecouteau, E., Polenta, G., Pratt, G. W., Prunet, S., Puget, J. L., Rachen, J. P., Reinecke, M., Remazeilles, M., Renault, C., Renzi, A., Ristorcelli, I., Rocha, G., Rosset, C., Rossetti, M., Roudier, G., Rubiño-Martín, J. A., Rusholme, B., Sandri, M., Santos, D., Savelainen, M., Savini, G., Scott, D., Spencer, L. D., Stolyarov, V., Stompor, R., Sudiwala, R., Sunyaev, R., Suur-Uski, A. S., Sygnet, J. F., Tauber, J. A., Terenzi, L., Toffolatti, L., Tomasi, M., Tristram, M., Tucci, M., Türler, M., Umana, G., Valenziano, L., Valiviita, J., Van Tent, F., Vielva, P., Villa, F., Wade, L. A., Wandelt, B. D., Wehus, I. K., Welikala, N., Yvon, D., Zacchei, A., and Zonca, A. (2016). Planck intermediate results. XXXIX. The Planck list of high-redshift source candidates. , 596:A100.

Planck Collaboration, Aghanim, N., Altieri, B., Arnaud, M., Ashdown, M., Aumont, J., Baccigalupi, C., Banday, A. J., Barreiro, R. B., Bartolo, N., Battaner, E., Beelen, A., Benabed, K., Benoit-Lévy, A., Bernard, J. P., Bersanelli, M., Bethermin, M., Bielewicz, P., Bonavera, L., Bond, J. R., Borrill, J., Bouchet, F. R., Boulanger, F., Burigana, C., Calabrese, E., Canameras, R., Cardoso, J. F., Catalano, A., Chamballu, A., Chary, R. R., Chiang, H. C., Christensen, P. R., Clements, D. L., Colombi, S., Couchot, F., Crill, B. P., Curto, A., Danese, L., Dassas, K., Davies, R. D., Davis, R. J., de Bernardis, P., de Rosa, A., de Zotti, G., Delabrouille, J., Diego, J. M., Dole, H., Donzelli, S., Doré, O., Douspis, M., Ducout, A., Dupac, X., Efstathiou, G., Elsner, F., Enßlin, T. A., Falgarone, E., Flores-Cacho, I., Forni, O., Frailis, M., Fraisse, A. A., Franceschi, E., Frejsel, A., Frye, B., Galeotta, S., Galli, S., Ganga, K., Giard, M., Gjerløw, E., González-Nuevo, J., Górski, K. M., Gregorio, A., Gruppuso, A., Guéry, D., Hansen, F. K., Hanson, D., Harrison, D. L., Helou, G., Hernández-Monteagudo, C., Hildebrandt, S. R., Hivon, E., Hobson, M., Holmes, W. A., Hovest, W., Huffenberger, K. M., Hurier, G., Jaffe, A. H., Jaffe,

- T. R., Keihänen, E., Keskitalo, R., Kisner, T. S., Kneissl, R., Knoche, J., Kunz, M., Kurki-Suonio, H., Lagache, G., Lamarre, J. M., Lasenby, A., Lattanzi, M., Lawrence, C. R., Le Floc'h, E., Leonard, R., Levrier, F., Liguori, M., Lilje, P. B., Linden-Vørnle, M., López-Caniego, M., Lubin, P. M., Macías-Pérez, J. F., MacKenzie, T., Maffei, B., Mandolesi, N., Maris, M., Martin, P. G., Martinache, C., Martínez-González, E., Masi, S., Matarrese, S., Mazzotta, P., Melchiorri, A., Mennella, A., Migliaccio, M., Moneti, A., Montier, L., Morgante, G., Mortlock, D., Munshi, D., Murphy, J. A., Natoli, P., Negrello, M., Nesvadba, N. P. H., Novikov, D., Novikov, I., Omont, A., Pagano, L., Pajot, F., Pasian, F., Perdereau, O., Perotto, L., Perrotta, F., Pettorino, V., Piacentini, F., Piat, M., Plaszczynski, S., Pointecouteau, E., Polenta, G., Popa, L., Pratt, G. W., Prunet, S., Puget, J. L., Rachen, J. P., Reach, W. T., Reinecke, M., Remazeilles, M., Renault, C., Ristorcelli, I., Rocha, G., Roudier, G., Rusholme, B., Sandri, M., Santos, D., Savini, G., Scott, D., Spencer, L. D., Stolyarov, V., Sunyaev, R., Sutton, D., Sygnet, J. F., Tauber, J. A., Terenzi, L., Toffolatti, L., Tomasi, M., Tristram, M., Tucci, M., Umana, G., Valenziano, L., Valiviita, J., Valtchanov, I., Van Tent, B., Vieira, J. D., Vielva, P., Wade, L. A., Wandelt, B. D., Wehus, I. K., Welikala, N., Zacchei, A., and Zonca, A. (2015). Planck intermediate results. XXVII. High-redshift infrared galaxy overdensity candidates and lensed sources discovered by Planck and confirmed by Herschel-SPIRE. , 582:A30.
- Poggianti, B. M., Smail, I., Dressler, A., Couch, W. J., Barger, A. J., Butcher, H., Ellis, R. S., and Oemler, Augustus, J. (1999). The Star Formation Histories of Galaxies in Distant Clusters. , 518(2):576–593.
- Polletta, M., Dole, H., Martinache, C., Lehnert, M. D., Frye, B. L., and Kneissl, R. (2022). Molecular gas properties of Planck-selected protocluster candidates at $z = 1.3\text{--}3$. , 662:A85.
- Polletta, M., Soucail, G., Dole, H., Lehnert, M. D., Pointecouteau, E., Vietri, G., Scudiego, M., Montier, L., Koyama, Y., Lagache, G., Frye, B. L., Cusano, F., and Fumana, M. (2021). Spectroscopic observations of PHz G237.01+42.50: A galaxy protocluster at $z = 2.16$ in the Cosmos field. , 654:A121.
- Rettura, A., Rosati, P., Nonino, M., Fosbury, R. A. E., Gobat, R., Menci, N., Strazzullo, V., Mei, S., Demarco, R., and Ford, H. C. (2010). Formation Epochs, Star Formation Histories, and Sizes of Massive Early-Type Galaxies in Cluster and Field Environments at $z = 1.2$: Insights from the Rest-Frame Ultraviolet. , 709(1):512–524.
- Secrest, N. J., Dudik, R. P., Dorland, B. N., Zacharias, N., Makarov, V., Fey, A., Frouard, J., and Finch, C. (2015). Identification of 1.4 Million Active Galactic Nuclei in the Mid-Infrared using WISE Data. , 221(1):12.
- Shimakawa, R., Koyama, Y., Röttgering, H. J. A., Kodama, T., Hayashi, M., Hatch, N. A., Dannerbauer, H., Tanaka, I., Tadaki, K.-i., Suzuki, T. L., Fukagawa, N., Cai, Z., and Kurk, J. D. (2018). MAHALO Deep Cluster Survey II.

- Characterizing massive forming galaxies in the Spiderweb protocluster at $z = 2.2.$, 481(4):5630–5650.
- Stern, D., Assef, R. J., Benford, D. J., Blain, A., Cutri, R., Dey, A., Eisenhardt, P., Griffith, R. L., Jarrett, T. H., Lake, S., Masci, F., Petty, S., Stanford, S. A., Tsai, C.-W., Wright, E. L., Yan, L., Harrison, F., and Madsen, K. (2012). Mid-infrared Selection of Active Galactic Nuclei with the Wide-Field Infrared Survey Explorer. I. Characterizing WISE-selected Active Galactic Nuclei in COSMOS. , 753(1):30.
- Umehata, H., Tamura, Y., Kohno, K., Ivison, R. J., Alexander, D. M., Geach, J. E., Hatsukade, B., Hughes, D. H., Ikarashi, S., Kato, Y., Izumi, T., Kawabe, R., Kubo, M., Lee, M., Lehmer, B., Makiya, R., Matsuda, Y., Nakanishi, K., Saito, T., Smail, I., Yamada, T., Yamaguchi, Y., and Yun, M. (2015). ALMA Deep Field in SSA22: A Concentration of Dusty Starbursts in a $z = 3.09$ Protocluster Core. , 815(1):L8.
- Véron-Cetty, M. P. and Véron, P. (2010). A catalogue of quasars and active nuclei: 13th edition. , 518:A10.
- Waldrop, M. M. (1983). The large-scale structure of the universe. *Science*, 219(4588):1050–1052.
- Wright, E. L., Eisenhardt, P. R. M., Mainzer, A. K., Ressler, M. E., Cutri, R. M., Jarrett, T., Kirkpatrick, J. D., Padgett, D., McMillan, R. S., Skrutskie, M., Stanford, S. A., Cohen, M., Walker, R. G., Mather, J. C., Leisawitz, D., Gautier, Thomas N., I., McLean, I., Benford, D., Lonsdale, C. J., Blain, A., Mendez, B., Irace, W. R., Duval, V., Liu, F., Royer, D., Heinrichsen, I., Howard, J., Shannon, M., Kendall, M., Walsh, A. L., Larsen, M., Cardon, J. G., Schick, S., Schwalm, M., Abid, M., Fabinsky, B., Naes, L., and Tsai, C.-W. (2010). The Wide-field Infrared Survey Explorer (WISE): Mission Description and Initial On-orbit Performance. , 140(6):1868–1881.
- Wu, J., Jun, H. D., Assef, R. J., Tsai, C.-W., Wright, E. L., Eisenhardt, P. R. M., Blain, A., Stern, D., Díaz-Santos, T., Denney, K. D., Hayden, B. T., Perlmutter, S., Aldering, G., Boone, K., and Fagrelius, P. (2018). Eddington-limited Accretion in $z \sim 2$ WISE-selected Hot, Dust-obscured Galaxies. , 852(2):96.